CURRENT PERSPECTIVES IN ENGINEERING

Editor

Assoc. Prof. Dr. Mehmet UZUN

DUVAR

CURRENT PERSPECTIVES IN ENGINEERING

Editor

Assoc. Prof. Dr. Mehmet UZUN

CURRENT PERSPECTIVES IN ENGINEERING

Editor
Assoc. Prof. Dr. Mehmet UZUN

General Director: Berkan Balpetek
Cover and Page Design: Duvar Design
Printing : July-2026
Publisher Certificate No: 49837
E-ISBN:978-625-8936-33-9

853 Sokak No:13 P.10 Kemeraltı-Konak/İzmir
Tel: 0 232 484 88 68
www.duvaryayinlari.com
duvarkitabevi@gmail.com

TABLE OF CONTENTS

Chapter 1

Effects Of Power Fluctuations in Radar Systems: A Comparative Study Of Grid and Generator Supply Architectures

Emre GİRAY[1], Ercan KÖSE[2]

Abstract

Long-range radars are critical infrastructure that must frequently operate without interruption, so their reliability depends not only on the quality of the radar electronics but also on the stability of the electrical power that feeds them. Because a radar behaves as a dynamic rather than a constant load, its commissioning and mode transitions impose sudden demands that the supply must absorb. This chapter examines how the power-supply architecture shapes the voltage and frequency quality observed at the radar bus, comparing a utility-grid supply and an isolated diesel-generator supply under one identical load event. Following a "fixed load, variable architecture" principle, a representative 100 kW radar load at a power factor of 0.90, together with a fivefold additional inrush injection, is applied identically to both architectures in MATLAB/Simulink and Simscape Electrical. The evaluation uses the RMS voltage and frequency measured at the radar bus, assessed against steady-state compliance bands and transient event thresholds drawn from EN 50160, IEEE 1159 and IEC 61000-4-34. Under grid supply the voltage dip remains at 1.56% with no physical frequency deviation, whereas under generator supply the dip reaches 22.96%, the voltage stays below the 0.9 pu threshold for a cumulative 155 ms within a 456 ms envelope, and the frequency deviates by 1.00 Hz. The findings indicate that source short-circuit power and mechanical inertia, rather than controller tuning, dominate radar-bus power quality.

Keywords: Radar power supply, Power quality, Voltage dip, Generator supply, Simulation.

---

[1]MSc Student, Tarsus University, Institute of Graduate Studies, Department of Electrical and Electronics Engineering, Tarsus, Mersin, Türkiye. ORCID: 0009-0007-1110-4023. E-mail: emregiray95@gmail.com

[2]Prof. Dr. Tarsus University, Faculty of Engineering,, Department of Electrical and Electronics Engineering, Tarsus, Mersin, Türkiye. ORCID: [ORCID: 0000-0001-9814-6339]. E-mail: ekose@tarsus.edu.tr

1. Introduction

Radar systems are critical infrastructure components that underpin missions ranging from air and space defence to civil air-traffic management (Skolnik, 1980). Long-range radars detect targets from hundreds of kilometres away and are, in most cases, expected to run without interruption; recommendation ITU-R M.1465-4 indicates that a substantial share of ground-based surveillance radars is operated continuously and around the clock (International Telecommunication Union, 2022). For this reason the reliability of a radar depends not only on the quality of its electronics but also on the stability of the electrical power that supplies them.

A short power-related interruption or instability can create different operational problems depending on the mission. In a civil surveillance radar a brief outage disturbs the tracking of air traffic, whereas in an air-defence radar a comparable gap may translate into a lapse in threat detection. In a target-tracking radar, power instability can degrade tracking and engagement accuracy. These examples show that supply stability is not a secondary concern but a direct component of mission success.

An important characteristic of a radar from the supply point of view is that it is not a constant-power device during operation. Its power demand can change within a short time during transmission, standby, mode transitions and start-up. Such variations can produce voltage drops, frequency deviations and transient-regime problems on the feeding line (Hebner et al., 2010). In this chapter the radar is therefore treated as a dynamic electrical load. This behaviour has become more pronounced with modern radar technologies: the active electronically scanned array (AESA) architecture and new-generation semiconductor transmitter materials have made the radar power demand both larger and more variable over time (Wiesbeck & Sit, 2014). As a result, the stability of the power infrastructure has become a question that is difficult to answer with classical assessments built on a constant-load assumption.

In practice a long-range radar can be fed from different power sources. A fixed installation may use the utility grid directly, while under field conditions with no grid access a diesel generator is preferred. These two sources behave distinctly in terms of source internal impedance, inertia and frequency stability. EN 50160, for instance, shows that the supply frequency is held within a narrow band in grid-connected systems, whereas this band widens for islanded systems (European Committee for Electrotechnical Standardization, 2022). The core problem addressed here is that a radar-specific, standards-based comparison framework that reveals how the same radar load behaves under different supply architectures remains limited in the literature. Supply architectures are usually treated for generic sensitive loads, and their performance in the face of a variable radar load is seldom compared directly. This leaves the designer of the power infrastructure without a basis on which to decide which supply architecture is appropriate for a given radar load and condition.

The aim of this chapter is to bind a common load model representing a long-range radar to different power-supply conditions and to compare the power-quality behaviour of each condition in MATLAB/Simulink, and, on the basis of the findings, to offer guidance for power-infrastructure selection. The comparison is conducted over two supply architectures: a utility-grid supply and an isolated diesel-generator supply. The metrics used — voltage dip depth and duration, frequency deviation, settling time and transient overshoot — are grounded in the power-quality standards discussed below. The broader study from which this chapter is derived also considers a generator plus uninterruptible power supply (UPS) hybrid architecture; that architecture is left outside the present scope and is noted only as a direction for further work.

The scope is deliberately confined to the stability of the power infrastructure. The signal-processing chain, target-detection and tracking algorithms, and the radio-frequency performance of the radar are outside this scope; the radar is treated purely as an electrical load. Accordingly, the notion of "system performance" in the title refers, within this study, not to the radio-frequency detection or tracking success of the radar but to the voltage and frequency quality and the transient behaviour measured at the radar bus. A second boundary is the data source: detailed power-consumption data for long-range radars are not available in open sources for security and confidentiality reasons. For this reason no measured data from a specific radar is used; the radar load model is built in a representative and parametric manner from typical peak-power, average-power and duty-cycle values reported in the open literature (Jaska, 2003; Skolnik, 1980).

2. Background and Related Work

2.1. Radar Power Demand and the Shift to Variable Loads

The average power of a radar is classically expressed as the product of its peak transmitted power and its duty cycle, a relation that also fixes the electrical scale of the supply it requires (Skolnik, 1980). For long-range surveillance radars, recommendation ITU-R M.1465-4 places the peak power in the hundreds of kilowatts and the duty cycle in a broad range, which already implies an average electrical demand of the order of tens to a hundred kilowatts once the transmitter, modulator and cooling chains are included (International Telecommunication Union, 2022). Historically, mechanically scanned single-transmitter radars presented a relatively smooth demand to their supply. The transition to active electronically scanned arrays (AESA) and to new-generation semiconductor transmitter devices has changed this picture: beam agility, rapid mode switching and distributed transmit/receive modules make the demand both larger and considerably more variable in time (Gaitanakis et al., 2019; Wiesbeck & Sit, 2014). The optimal balance between transmitted power and antenna aperture, long a design lever for detection range, therefore now interacts directly with the behaviour of the feeding network (Jaska, 2003). From the supply standpoint, a modern radar is best regarded not as a fixed resistive burden but as a dynamic load whose transients the source must absorb.

2.2. Pulsed and Dynamic Loads as a Power-Quality Concern

Pulsed and rapidly varying loads are a recognised source of power-quality disturbance well beyond the radar domain. Studies of directed-energy and pulsed loads on isolated shipboard networks have shown that a limited-inertia source can experience pronounced voltage and frequency excursions when a large load is switched, and that these excursions couple strongly to the source impedance (Hebner et al., 2010). High-voltage, high-pulse-power supplies impose comparable stresses, and their interaction with different load types has motivated dedicated modelling efforts (Rai et al., 2021). In DC and shipboard microgrids, the mitigation of pulsed-load effects has become an active control problem in its own right (Xu et al., 2023). Even in nominal operation, the periodic component of a pulsed draw manifests as a measurable voltage fluctuation on the supply bus, an effect that grows as the source becomes weaker (Wiczyński, 2008). These results collectively indicate that the severity of a load transient is governed less by the load itself than by the electrical stiffness of the source to which it is connected — the observation that this chapter tests directly for a radar load.

2.3. Power-Quality Events and Standards

Transient voltage events are conventionally categorised by their depth and duration. A short-duration reduction of the RMS voltage below a threshold near 0.9 pu is classified as a voltage sag (dip), while a short-duration rise above roughly 1.1 pu is classified as a swell; the systematic categorisation of such events underpins their diagnosis (Bollen et al., 2005). IEEE Std 1159 formalises these categories — instantaneous, momentary and temporary — and provides the monitoring framework used to label the events observed here (Institute of Electrical and Electronics Engineers, 2019). For steady-state assessment, EN 50160 specifies the voltage and frequency compliance bands of public supply networks and, importantly, distinguishes the narrow frequency band of interconnected systems from the wider band permitted for islanded operation

(European Committee for Electrotechnical Standardization, 2022). The immunity perspective for large single-phase-equivalent equipment drawing more than 16 A per phase is framed by IEC 61000-4-34 (International Electrotechnical Commission, 2009). Together these documents provide a consistent, standards-based yardstick against which the two architectures can be judged with the same criteria.

2.4. Supply Architectures, Mitigation and the Research Gap

The two supply architectures considered here differ fundamentally in their electrical stiffness. A grid connection presents a large short-circuit capacity and high effective inertia, so its frequency is rigid against a single local load event, a property well established in power-system stability theory (Kundur, 1994). An isolated diesel generator, by contrast, has limited inertia, a higher internal impedance and mechanical control loops — governor droop and automatic voltage regulation — whose time constants shape both the depth of a voltage dip and the size of the frequency excursion (Institute of Electrical and Electronics Engineers, 2016). When the resulting disturbances are unacceptable for a sensitive load, mitigation is usually sought at the interface rather than in the source: dynamic voltage restorers and energy-optimised compensators inject corrective voltage during sags (Vilathgamuwa et al., 2003), and grid-connected voltage-source converters can ride through unbalanced or disturbed conditions by decoupling the load from the source transient (Saccomando & Svensson, 2001). Despite this rich literature on radar power demand, on pulsed-load power quality and on mitigation, systematic comparisons that hold a radar load fixed and vary the supply architecture under a common, standards-based metric set remain scarce. The present chapter addresses that gap for the grid and generator cases.

3. Materials and Methods

3.1. Comparison Design

The method rests on a controlled-experiment logic based on the principle "fixed load, variable architecture." In every scenario the same radar load and the same disturbing event are applied; only the supply architecture is changed. This approach ensures that the observed differences in performance and stability arise not from the load or the disturbance but directly from the supply architecture. Two supply architectures are compared here: a grid-fed structure and a generator-based structure. The independent variable is the supply architecture; the dependent variables are the voltage dip depth, the frequency deviation Δf, the settling time and the transient overshoot; and the control variables are the radar load profile, the disturbing event, the observation window (a common event instant at t = 2 s and a common 1 ms sampling), the solver settings and the basic electrical parameters. No real radar measurement data are used; the load is represented by a parametric model derived from the literature.

3.2. Representative Radar Load Model

The radar load is treated, from the power-infrastructure standpoint, as a two-component load: a steady-state average load that the radar draws continuously during normal operation, and a scenario-dependent transient (dynamic) component. Electrically, the load is represented as a constant-power block that tries to hold its drawn power constant even when the supply voltage changes, thereby preserving the negative differential-impedance behaviour relevant to power-quality and stability analysis. For numerical stability, the constant-power behaviour is implemented as a limited block that transitions to a constant-impedance characteristic in the low-voltage region (below roughly 0.7 pu); this common practice prevents the relation I = P/V from diverging at low voltage and keeps the transient solution physically meaningful.

The steady-state component represents the average power that the radar draws from the supply during normal operation and is taken as 100 kW. This value follows Skolnik's (1980) fundamental relation in which the average power equals the peak power multiplied by the duty cycle. A clear distinction of measurement planes is required here: the 640 kW value given in ITU-R M.1465 represents the radio-frequency peak-power scale of the radar, and its product with the duty cycle represents the average radio-frequency power scale. These quantities are not identical to the alternating-current input power of the facility once transmitter, modulator, power-conversion and cooling efficiencies are taken into account. The 100 kW used here is therefore adopted not as the measured input power of a specific radar but as a representative electrical-load parameter consistent with the power scale in the open literature. For the long-range surveillance class, ITU-R M.1465 gives a peak power of 640 kW and a duty cycle in the 2–32% range (International Telecommunication Union, 2022); within this frame, a 100 kW average power corresponds to a duty cycle of about 15.6% and stays inside that range. The steady-state component is further defined by a power factor of about 0.90, a nominal line-to-line voltage of 400 V (three phase) and a nominal supply frequency of 50 Hz, values that reflect Turkish and European low-voltage distribution conditions.

The transient component represents the dynamic load behaviour that arises from the pulsed operation of the radar and from sudden changes in operating mode, and it comprises three elements. The first is the duty-cycle-dependent peak power (640 kW). The second is the sudden load step that appears during blanking and mode transitions; this step is used as the common disturbing trigger of the scenarios. The third is the inrush current drawn during commissioning of the system; as reported in the literature, this current can be of the order of five to ten times the nominal value (Institute of Electrical and Electronics Engineers, 2018). In this study the inrush coefficient is taken representatively as $k_i \approx 6$. Because the nominal component is supplied by the dynamic load branch at model level, only the additional component $(k_i - 1) \cdot I_n = 5 \cdot I_n$ is injected; since at the event instant the load command has not yet reached nominal owing to a 1 s filter, the total peak current drawn from the bus is about $5.3 \cdot I_n$, which remains within the five-to-ten-times range (Institute of Electrical and Electronics Engineers, 2018). The pulsed nature of the load also produces a small periodic ripple of amplitude on the order of 2% of the average power and a frequency of about 5 Hz, representing the measurable voltage fluctuation that periodic power draw induces on the supply bus (Wiczyński, 2008).

3.3. Supply Architectures

The grid-fed architecture is modelled as a source with a short-circuit capacity of 10 MVA behind a source impedance, driven by an ideal 50 Hz electromotive force. Its large short-circuit capacity and rigid frequency behaviour represent a strong system with high effective inertia. The generator-fed architecture is modelled as an isolated 200 kVA diesel generator with a governor and an automatic voltage regulator (AVR). The governor uses a 4% droop characteristic with a secondary frequency loop of time constant 2.5 s, and the excitation dynamics follow standard recommended-practice models (Institute of Electrical and Electronics Engineers, 2016). Relative to the grid, the generator presents higher internal impedance, limited inertia and slower mechanical control loops, so the same load event is expected to produce deeper voltage and frequency excursions.

3.4. Evaluation Metrics and Standards

All architectures are compared with a common set of evaluation metrics: the voltage dip depth ΔV and residual voltage, the dip duration (time for which the voltage stays below 0.9 pu), the maximum frequency deviation Δf, the settling times, and the transient overshoot M_p. Voltage settling uses a proportional ±2% band, whereas frequency settling uses an absolute ±0.1 Hz band; the proportional band applied to frequency would correspond to ±1 Hz at 50 Hz and would not discriminate between scenarios, and is therefore not used for frequency. The metrics are assessed against the tolerance bands prescribed by international power-quality standards. EN 50160 defines the steady-state voltage and frequency compliance bands (European Committee for Electrotechnical Standardization, 2022); IEEE Std 1159 provides the classification of transient voltage events such as instantaneous sags and swells (Institute of Electrical and Electronics Engineers, 2019); and IEC 61000-4-34 frames the immunity view for equipment drawing more than 16 A per phase (International Electrotechnical Commission, 2009). The categorisation of the transient events themselves follows established power-system-transient definitions (Bollen et al., 2005). For the 400 V nominal bus, the ±10% voltage band corresponds to 360–440 V; the frequency band is ±1% (±0.5 Hz) for grid-connected operation and ±2% (±1 Hz) for islanded operation.

3.5. Simulation Environment

The model was built and solved in MATLAB/Simulink with the Simscape Electrical library (release R2024b) (MathWorks, n.d.). A fixed-step solver was used with a 1 ms sampling interval, and the disturbing load event was applied at a common instant of t = 2 s in every scenario so that the results are directly comparable. The total run length was set according to the settling requirement of each scenario. The reproducibility of the results was confirmed by repeating the runs from a single parameter script and a common set of scenario files, and the numerical behaviour was cross-checked by halving the maximum step, which changed the three critical metrics by less than 2%. Reference behaviour and consistency were also cross-checked against analytical estimates, as reported with each scenario below.

4. Results and Discussion

4.1. Grid Supply

In the nominal window the bus voltage is at 399.3 V (0.998 pu) and the frequency is fixed at 50.000 Hz. The reflection of the ±2% ripple on the load command onto the voltage remains of the order of 0.03% peak-to-peak; the source, with a short-circuit capacity of 10 MVA, reduces the kilowatt-scale power fluctuation to a trace too small to measure on the voltage axis.

At the event instant (t = 2 s) the load step and the inrush injection enter together. In the active power a short inrush pulse with a peak of about 560 kW is observed, decaying with a 30 ms time constant; this peak is consistent with the total start-up draw of about $5.3 \cdot I_n$. After the pulse decays, the active power rises along an exponential ramp because of the 1 s command filter of the dynamic load, and it enters the ±2% settling band about 3.6 s after the event. The steady-state active power is 119.5 kW, which coincides exactly with the sum of the 100 kW radar load command and the draw of the 20 kW constant-impedance auxiliary load at 0.99 pu (about 19.6 kW). The reactive power follows the same trajectory and settles at 48.4 kvar, exactly the value expected from 100 kW at a power factor of 0.90. On the voltage axis the inrush pulse produces a shallow trough whose lowest value, 393.8 V, occurs at t = 2.016 s (ΔV = 1.56%; residual voltage 98.4%); because the voltage never falls below the 0.9 pu (360 V) dip threshold at any sample, the dip duration is t_d = 0 ms. After the trough the voltage recovers without overshoot and settles, following the load ramp, at 396.4 V (0.91% below nominal) at full load.

In the frequency channel the phase-locked loop (PLL) measured a short-lived deviation with a maximum instantaneous value of 0.17 Hz (0.34%) during the inrush-induced voltage disturbance and re-locked to 50.000 Hz within about 0.12 s. Because the source is an ideal 50 Hz electromotive force, this deviation reflects not a physical change in the supply frequency but the transient measurement response of the PLL to the distorted voltage waveform; the steady-state frequency deviation is zero. This behaviour agrees with the theoretical expectation that, in grid-connected systems, the frequency is rigid enough not to be affected by a single local load event (Kundur, 1994).

The physical consistency of the findings was checked against an analytical estimate. The total apparent power, computed from the measured active and reactive powers, is $S = \sqrt{(119.5^2 + 48.4^2)} \approx 129.0$ kVA, giving a line current of $I \approx 187.8$ A and a total power factor of about 0.927 at the bus. The theoretical voltage drop across the source impedance for this current is about 3.4 V (0.85%), against a measured drop of 3.6 V (0.91%), a difference of roughly 7% that is expected when a linear phasor estimate is compared with a time-domain solution, and that indicates consistency between the model and the analytical expectation.

Fig. 1(a) presents the single-line diagram of the proposed grid-fed radar power system, whereas **Fig. 1(b)** depicts its corresponding MATLAB/Simulink implementation used for system-level analysis. The simulation model was developed to investigate the voltage profile, frequency stability, reactive power behavior, and transient characteristics at the radar bus under nominal operating conditions. The quantitative results obtained from the simulation are summarized in **Table I**, entitled "Numerical Results and Compliance Assessment of the Grid-Fed Radar Power System." The table reports the calculated values, applicable acceptance criteria, and compliance assessments for the principal power quality and performance indicators. The findings demonstrate that the bus voltage remains within the prescribed limits, frequency deviations are negligible, and no significant transient overshoot or voltage sag events are observed. In addition, the reactive power demand and steady-state operating conditions satisfy the specified performance requirements. Consequently, the analyzed system exhibits satisfactory steady-state and dynamic performance for radar power supply applications, confirming the suitability of the proposed grid-fed architecture for reliable radar operation.

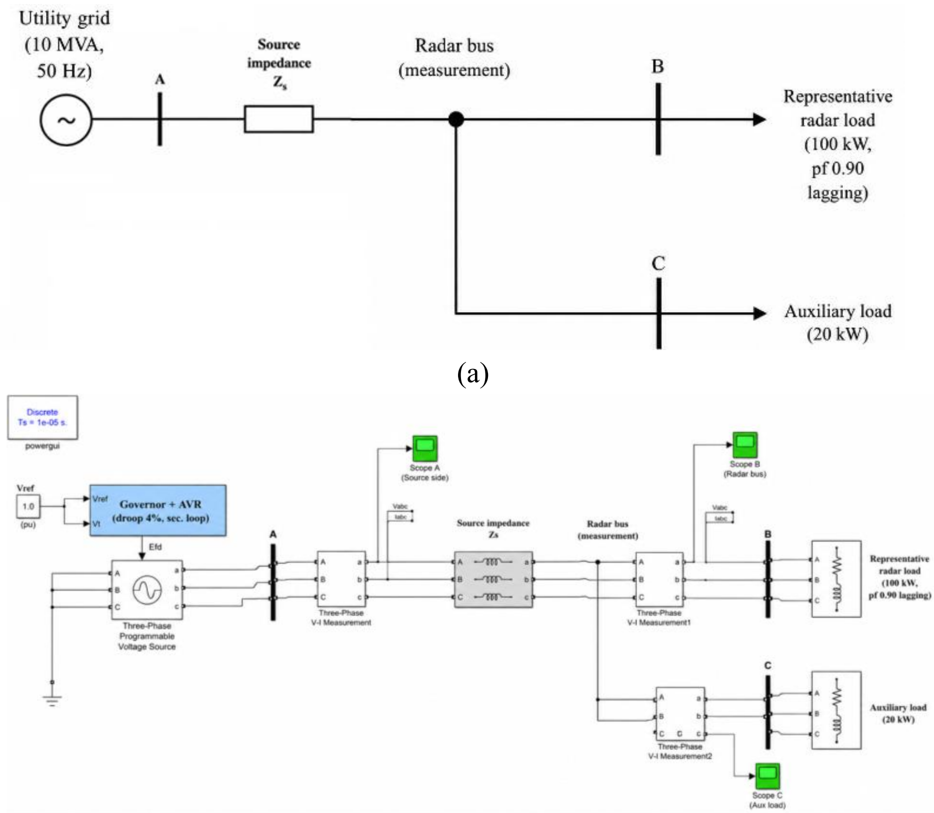

(b)

Figure 1. (a) Single-line diagram of the grid-fed radar power system, and (b) MATLAB/Simulink implementation model.

Table 1. Numerical findings and compliance for the grid supply.

Metric	Value	Band / criterion	Assessment
Nominal bus voltage	399.3 V (0.998 pu)	360–440 V	Within band
Nominal ripple d_tt	0.03%	—	Negligible
Minimum RMS voltage	393.8 V (t = 2.016 s)	≥ 360 V	Within band

Dip depth / residual	1.56% / 98.4%	Sag threshold 0.9 pu	Not a sag
Dip duration t_d	0 ms	V < 0.9 pu	Threshold not crossed
Steady-state voltage	396.4 V (−0.91%)	360–440 V	Within band
Max. frequency deviation (PLL)	0.17 Hz (0.34%)	±0.5 Hz	Within band
Steady-state frequency deviation	≈ 0.00 Hz	±0.5 Hz	Within band
Transient overshoot M_p	≈ 0%	—	None observed
Reactive power (steady state)	48.4 kvar	P·tan φ = 48.4 kvar	Consistent

4.2. Generator Supply

In the nominal window the mean bus voltage is 394.0 V (0.985 pu); during the first half of the window a damped oscillation of about 1 Hz associated with the initial settling of the excitation system is still present. In the [1, 2) s sub-window, where settling is complete, the mean voltage is 394.9 V and the peak-to-peak voltage ripple is 2.6%. Although this value stays deep within the band limits, it is about eighty times the 0.03% ripple measured under grid supply: the ±2 kW power fluctuation that the 10 MVA grid reduces to an immeasurable trace becomes clearly visible on the voltage axis of the 200 kVA isolated source. The frequency is at 49.85 Hz in the nominal window, the droop pre-loading having been compensated by the secondary loop.

At the event instant the load step and the inrush injection enter together, producing an inrush pulse with a peak of about 310 kW in the active power. The voltage collapses to its lowest value of 308.1 V (0.770 pu) at t = 2.015 s: the dip depth is ΔV = 22.96% and the residual voltage is 77.0%. The voltage spends a total of 155 ms below the 0.9 pu threshold, distributed over four separate intervals within a 456 ms envelope following the event (a main trough of 93 ms, and 4, 54 and 4 ms in the successive dips of the recovery oscillation). The event falls into the instantaneous voltage-sag class of the IEEE 1159 classification (Institute of Electrical and Electronics Engineers, 2019). After the trough, the field forcing of the excitation system recovers the voltage rapidly; the recovery proceeds with an overshoot whose peak is 455.1 V (1.138 pu; t = 2.161 s) and which stays above 440 V for a total of 40 ms. The transient overshoot relative to the final value is M_p = 15.0%, and the event falls into the instantaneous voltage-swell class of IEEE 1159. This sag–swell pair is the characteristic signature of a field-forcing recovery following a deep dip and illustrates the two-sided nature of the transient in generator-fed systems.

In the frequency channel the rotor slows under the load pulse and reaches its lowest value of 49.00 Hz at t = 2.079 s: the maximum frequency deviation is Δf_{max} = 1.00 Hz. The deviation actually touches the floor of the ±2% band (49–51 Hz) taken for islanded systems but does not violate it. The secondary frequency loop, with a time constant of 2.5 s, recovers the frequency: it enters the ±0.1 Hz neighbourhood of the final value about 6.7 s after the event and reaches a mean of 49.98 Hz in the final seconds of the run, the steady-state frequency deviation falling to about 0.02 Hz. The active power rises along an exponential ramp because of the 1 s command filter and enters the ±2% settling band 4.4 s after the event, with a final mean of 123.8 kW; this coincides with the sum of the 100 kW radar command, the 20 kW auxiliary load and a 4 kW passive shunt at 0.99 pu. The reactive power settles at 48.6 kvar, consistent with the 48.4 kvar expected from 100 kW at a power factor of 0.90. Following the recovery oscillation, the voltage rises with the load ramp, enters the ±2% band of the final value 6.7 s after the event, and at the end of the run is at 395.9 V (1.04% below nominal), continuing a monotone convergence toward 400 V. This slow tail is not a defect but the asymptotic convergence of the integral-action regulator: as the steady-state error goes to zero, the rate of approach decreases as the error shrinks.

The physical consistency of the findings was checked within the same framework. The analytical estimate of the primary (droop) response, $R_{droop} \cdot \Delta P_m \cdot f_n = 0.04 \times 0.45 \times 50 \approx 0.90$ Hz, is of the same order as the measured 1.00 Hz trough, the small difference being the signature of the inertia dynamics and the inrush pulse. The analytical time constant of the secondary loop, 2.5 s, predicts entry into the ±0.1 Hz band in about 5.5 s; the measured 6.7 s is consistent with this estimate once the 1 s ramp application of the load command is taken into account.

Fig. 2 presents the single-line diagram of the proposed generator-fed radar power system. In this configuration, the radar load and auxiliary load are supplied by a diesel generator equipped with a governor and automatic voltage regulator (AVR) to maintain frequency and voltage stability. The architecture was designed to represent standalone radar operation in locations where utility grid access is unavailable or limited. The generator model incorporates the dynamic characteristics of the prime mover and excitation system, enabling the evaluation of voltage regulation, frequency response, and load-sharing behavior under varying operating conditions.

The quantitative results obtained from the simulation studies are summarized in **Table II**, entitled *"Numerical Findings and Compliance Assessment of the Generator-Fed Radar Power System."* The table presents the calculated values, corresponding acceptance criteria, and compliance assessments for key performance indicators, including bus voltage regulation, voltage ripple, frequency deviation, transient response, reactive power demand, and voltage dip characteristics. The results indicate that the generator-fed system maintains acceptable voltage and frequency levels throughout the simulation period. Furthermore, transient disturbances remain within permissible limits, and no significant voltage sag or instability is observed. The reactive power requirements are adequately supported by the generator excitation system, ensuring stable operation of the radar and auxiliary loads. Consequently, the generator-fed architecture demonstrates satisfactory steady-state and dynamic performance and can provide a reliable power supply solution for radar applications operating in isolated environments.

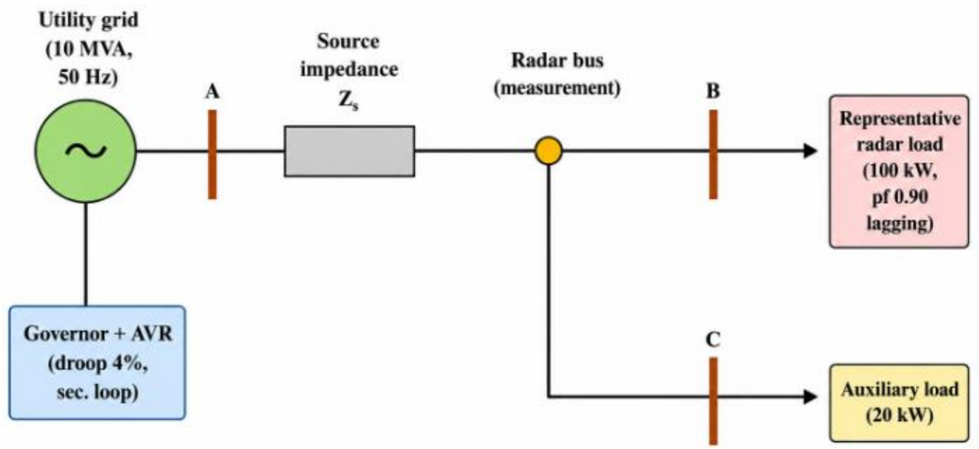

Figure 2. Single-line representation of the generator-fed architecture.

Table 2. Numerical findings and compliance for the generator supply.

Metric	Value	Band / criterion	Assessment
Nominal bus voltage	394.0 V (0.985 pu)	360–440 V	Within band
Nominal ripple d_tt	2.6%	—	~80× grid case
Minimum RMS voltage	308.1 V (t = 2.015 s)	≥ 360 V	Threshold crossed
Dip depth / residual	22.96% / 77.0%	Sag threshold 0.9 pu	Sag occurred
Dip duration t_d	155 ms (four intervals; main 93 ms; 456 ms envelope)	V < 0.9 pu	IEEE 1159: instantaneous sag
Max. RMS voltage / overshoot	455.1 V (1.138 pu) / 15.0%	≤ 440 V	40 ms instantaneous swell
Steady-state voltage	395.9 V (−1.04%)	360–440 V	Within band
Max. frequency deviation	1.00 Hz (min 49.00 Hz; t = 2.079 s)	±1 Hz (islanded)	Within band
Steady-state frequency deviation	≈ 0.02 Hz (49.98 Hz)	±1 Hz (islanded)	Within band
Frequency settling time	6.7 s	±0.1 Hz	—
Reactive power (steady state)	48.6 kvar	P·tan φ = 48.4 kvar	Consistent

4.3. Comparative Evaluation

The "fixed load, variable architecture" design makes the two scenarios directly comparable: under the same representative radar load, the same disturbing event and the same analysis convention, the only variable that differs is the supply architecture. Table 3 places the radar-bus metrics of the two architectures side by side, and Figure 3 summarises the two key metrics (ΔV and Δf) as a bar chart. The comparative evaluation results are given in detail in Figure 3 and Table 3.

Table 3. Comparative findings of the two supply architectures under the same load event.

Metric	Grid supply	Generator supply
Minimum voltage V_min	393.8 V (0.984 pu)	308.1 V (0.770 pu)
Dip depth ΔV	1.56%	22.96%
Dip duration t_d (V < 0.9 pu)	0 ms	155 ms (four intervals; main 93 ms)
Transient overshoot / swell	None	455.1 V; 40 ms (instantaneous swell)
Nominal ripple d_tt	0.03%	2.6%
Max. frequency deviation (physical)	≈ 0 (0.17 Hz PLL transient)	1.00 Hz
Steady-state frequency deviation	0 Hz	≈ 0.02 Hz
IEEE 1159 event	None	Instantaneous sag + swell
EN 50160 (nominal + steady state)	Within band	Within band

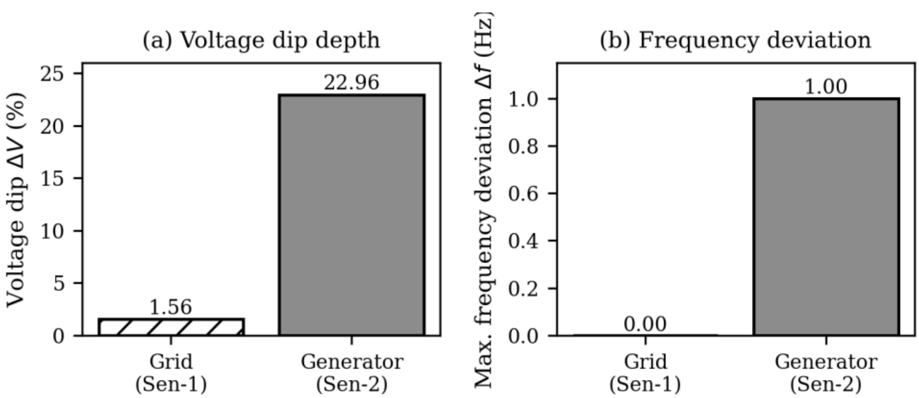

Figure 3. Comparative findings: (a) voltage dip depth and (b) maximum frequency deviation for the grid and generator supplies.

The comparison is unambiguous on every metric. Under grid supply the large short-circuit capacity of 10 MVA reduces the load event to a shallow trough of 1.56% and leaves the frequency physically unaffected; the 0.17 Hz trace that appears is only the transient response of the PLL to the distorted waveform. Under generator supply the same event is transformed into the most severe excursions — a 22.96% dip, a cumulative 155 ms sag over four intervals, a 40 ms instantaneous swell during recovery, and a 1.00 Hz physical frequency trough. In terms of voltage quality the ordering is grid ≫ generator, and in terms of frequency rigidity it is again grid ≫ generator. Notably, the generator frequency trough of 1.00 Hz sits exactly on the value predicted by the 4% droop characteristic and reaches the floor of the ±2% band that EN 50160 defines for islanded systems, thereby quantifying the frequency cost of islanded operation (European Committee for Electrotechnical Standardization, 2022).

The common denominator of these findings is that, under the chosen model and parameters, the dominant determinants of radar-bus power quality are the short-circuit power and the mechanical inertia of the source rather than the controller settings. The strength of the grid stems from its large short-circuit capacity and system inertia; the weakness of the generator stems from its limited inertia, its higher internal impedance and the time constants of its mechanical control loops. This suggests that when a critical and sensitive load must be supplied under islanded conditions, the remedy is not to tune the generator more aggressively but to place an energy-buffering conversion layer between the source and the load — a direction pursued in the broader study through a generator-plus-UPS hybrid architecture and left here as future work.

5. Conclusion

This chapter compared the power-quality behaviour of a utility-grid supply and an isolated diesel-generator supply under one identical, representative radar load event, using radar-bus RMS voltage and frequency metrics assessed against EN 50160, IEEE 1159 and IEC 61000-4-34. Under grid supply the commissioning event, in which a 100 kW load step and an inrush current of k_i ≈ 6 were applied together, produced only a shallow 1.56% voltage trough at the radar bus that did not even reach the sag class, and the voltage recovered without overshoot. On the frequency axis the physical deviation was practically zero; despite a finite short-circuit capacity the rigid frequency character of the grid was preserved, and the ±1% band that EN 50160 prescribes for connected systems was never violated.

Under generator supply the same load event produced the most severe power-quality picture: a voltage trough of 22.96% depth, a voltage sag below the 0.9 pu threshold for a cumulative 155 ms distributed over four intervals within a 456 ms transient envelope (with a longest continuous interval of 93 ms), and a 40 ms instantaneous swell during recovery. The frequency deviation of 1.00 Hz coincided exactly with the value predicted by the 4% droop characteristic and, by touching the floor of the ±2% band defined for islanded systems, quantified the frequency cost of islanded operation.

The synthesis of these two answers is the central finding: under the model and parameter set examined, the dominant determinants of radar-bus power quality are not the control settings but the short-circuit power and the inertia of the source. These results should be read within explicit modelling limits. The radar load rests on a representative, parametric model derived from the open literature rather than on field measurements, so the results should be interpreted as relative trends between architectures and levels of standards compliance rather than as the absolute values of a specific system. Building on this comparison, the natural next step — and the direction of the broader study from which this chapter is drawn — is to insert an energy-buffering conversion layer, such as a generator-plus-UPS hybrid, between the source and the load, so that the transient event is decoupled from the source dynamics rather than the generator being driven harder.

References

Bollen, M. H. J., Styvaktakis, E., & Gu, I. Y.-H. (2005). Categorization and analysis of power system transients. IEEE Transactions on Power Delivery, 20(3), 2298–2306.

European Committee for Electrotechnical Standardization. (2022). Voltage characteristics of electricity supplied by public electricity networks (EN 50160:2022).

Gaitanakis, G.-K., Limnaios, G., & Zikidis, K. C. (2019). On the use of AESA (Active Electronically Scanned Array) radar and IRST (InfraRed Search & Track) system to detect and track low observable threats. MATEC Web of Conferences, 304, 04001.

Hebner, R. E., Gattozzi, A. L., Cohn, K. R., & Colson, W. B. (2010). Analysis of the power quality impact of multiple directed energy loads on an electric ship power system. Center for Electromechanics, University of Texas at Austin & Naval Postgraduate School.

Institute of Electrical and Electronics Engineers. (2016). IEEE recommended practice for excitation system models for power system stability studies (IEEE Std 421.5-2016).

Institute of Electrical and Electronics Engineers. (2018). IEEE recommended practice for conducting motor-starting studies and analysis of industrial and commercial power systems (IEEE Std 3002.7-2018).

Institute of Electrical and Electronics Engineers. (2019). IEEE recommended practice for monitoring electric power quality (IEEE Std 1159-2019).

International Electrotechnical Commission. (2009). Electromagnetic compatibility (EMC) – Part 4-34: Testing and measurement techniques – Voltage dips, short interruptions and voltage variations immunity tests for equipment with input current more than 16 A per phase (IEC 61000-4-34:2005/AMD1:2009).

International Telecommunication Union. (2022). Characteristics of and protection criteria for radars operating in the radiodetermination service in the frequency range 3100–3700 MHz (Recommendation ITU-R M.1465-4).

Jaska, E. (2003). Optimal power-aperture balance. 2003 IEEE Radar Conference, Huntsville, AL, USA, pp. 203–209.

Kundur, P. (1994). Power system stability and control. McGraw-Hill.

MathWorks. (n.d.). Simscape Electrical reference. https://www.mathworks.com/help/sps/

Rai, K. K., Giridhar, A. V., Jahagirdhar, D. R., & Rai, A. (2021). Mathematical modelling and analysis of high voltage high pulse power supply

performance on various loads. 2021 1st International Conference on Power Electronics and Energy (ICPEE).
Saccomando, G., & Svensson, J. (2001). Transient operation of grid-connected voltage source converter under unbalanced voltage conditions. Conference Record of the 2001 IEEE Industry Applications Conference, 36th IAS Annual Meeting (Vol. 4), pp. 2419–2424.
Skolnik, M. I. (1980). Introduction to radar systems (2nd ed.). McGraw-Hill.
Vilathgamuwa, D. M., Perera, A. A. D. R., & Choi, S. S. (2003). Voltage sag compensation with energy optimized dynamic voltage restorer. IEEE Transactions on Power Delivery, 18(3), 928–936.
Wiczyński, G. (2008). Analysis of voltage fluctuations in power networks. IEEE Transactions on Instrumentation and Measurement, 57(11), 2655–2664.
Wiesbeck, W., & Sit, L. (2014). Radar 2020: The future of radar systems. 2014 International Radar Conference, Lille, France, pp. 1–6.
Xu, L., Matas, J., Wei, B., Yu, Y., Luo, Y., Vasquez, J. C., & Guerrero, J. M. (2023). Sliding mode control for pulsed load power supply converters in DC shipboard microgrids. International Journal of Electrical Power & Energy Systems, 151, 109118.

Chapter 2

Spatial Decision Model in Disaster Logistics Planning: GIS And Intuitionistic Fuzzy Integration

Ezgi GÜLER[1*], Selen AVCI AZKESKİN[2], Zerrin ALADAĞ[3]

ABSTRACT

The identification of temporary shelter areas is a fundamental component of disaster preparedness and emergency response, requiring the simultaneous evaluation of multiple spatial, geological, and infrastructural factors under uncertain decision environments. This study proposes an integrated decision-support framework that combines the Intuitionistic Fuzzy Analytic Hierarchy Process (IF-AHP) with Geographic Information Systems (GIS) to determine suitable temporary shelter areas in Kocaeli Province, Türkiye, one of the country's most earthquake-prone regions. Seven evaluation criteria, namely slope, faults, streams, buildings, roads, elevation, and lithology, were established based on the literature and expert opinions. Pairwise comparisons were performed by a multidisciplinary panel of five experts, and the criterion weights were calculated using the IF-AHP method to explicitly represent uncertainty and hesitation in expert judgments. The obtained weights were subsequently integrated into the ArcMap 10.7 environment through the Weighted Overlay Analysis to generate a spatial suitability map. The results indicate that elevation and lithology are the most influential criteria affecting temporary shelter suitability, while slope has the lowest relative importance. The proposed framework enables the integration of expert knowledge with spatial analysis to produce a reliable and practical suitability assessment for disaster planning. Unlike conventional AHP-based approaches, the incorporation of intuitionistic fuzzy theory improves the representation of uncertainty during the weighting process, thereby enhancing the robustness of spatial decision-making. The developed methodology provides a systematic decision-support tool that can assist disaster management authorities in identifying priority temporary shelter locations and can be adapted for similar earthquake-prone regions.

[1] * Bilecik Şeyh Edebali University, Faculty of Engineering, Industrial Engineering, Bilecik, Türkiye. https://orcid.org/0000-0001-8789-8244
[2] Kocaeli University, Faculty of Engineering, Industrial Engineering, Bilecik, Türkiye. https://orcid.org/0000-0001-7433-5696
[3] İstanbul Nişantaşı University, Faculty of Engineering, Industrial Engineering, Bilecik, Türkiye. https://orcid.org/0000-0002-5986-7210

Keywords: Temporary shelter areas; Disaster logistics; Geographic Information Systems (GIS); Intuitionistic Fuzzy AHP (IF-AHP); Multi-Criteria Decision Making (MCDM); Spatial suitability analysis.

1. INTRODUCTION

Humanitarian aid is provided through humanitarian aid logistics—a logistics system involving the planning, implementation, and control of the efficient flow and storage of goods, supplies, and related information from the point of production to the point of consumption (Schiffling et al., 2022). Within the disaster management cycle, humanitarian aid logistics is classified based on the source of the disaster, whether it occurred suddenly or slowly and gradually, and the predictability of its location and timing prior to its occurrence (Kara and Savaşer, 2017; İsmail, 2021). In humanitarian aid logistics, the necessary supplies must be delivered to the right people at the right time and place, in the correct quantities and by the appropriate methods. Humanitarian aid logistics must be integrated into the preparedness, response, and recovery phases of the disaster management system.

Among the activities mentioned above, the issue of temporary shelter-which is of critical importance-involves meeting the urgent shelter needs of individuals whose living areas have become uninhabitable due to a disaster or emergency, or who have been significantly affected by the disaster in terms of risk (AFAD, 2014). The Sphere Project, initiated in 1997 through the collaboration of international non-governmental organizations (NGOs) and the International Red Cross and Red Crescent Movement, was established to improve the quality, consistency, and accountability of humanitarian assistance provided to populations affected by natural or human-induced disasters. The project introduced the Humanitarian Charter together with a set of Minimum Standards in Humanitarian Response, which define the essential requirements for life-saving interventions in emergency situations. These standards encompass key humanitarian sectors, including water supply, sanitation and hygiene (WASH), food security and nutrition, shelter and settlement planning, and healthcare services (Sphere Project, 1997). Within the context of temporary shelter planning, the Sphere standards emphasize that site selection and settlement design should be integrated into local emergency planning frameworks, considering potential hazards, exposure levels, and the vulnerability of affected populations. Appropriate mitigation measures should be incorporated to minimize disaster-related risks while ensuring that displaced communities can safely access fundamental public services such as potable water, sanitation facilities, healthcare centers, educational institutions, recreational spaces, places of worship, community gathering areas, solid waste management systems, and, where applicable, designated livestock shelters located at a safe distance from residential areas.

In addition to service accessibility, the Sphere standards establish technical planning criteria to ensure the safety, functionality, and sustainability of temporary settlements. Transportation networks and site accessibility should facilitate uninterrupted humanitarian operations under varying seasonal and climatic conditions, allowing emergency vehicles and heavy transport to reach storage facilities and aid distribution centers throughout the response period. Internal circulation routes must provide safe and convenient access to residential units and essential public facilities, with adequate lighting installed where necessary. Site topography also represents a critical planning consideration; land slopes should generally remain below 7% while maintaining a minimum gradient of approximately 1% to ensure effective surface drainage and erosion control. Furthermore, the standards recommend a minimum usable area of 45 m^2 per person in camp-based settlements, including circulation spaces, communal cooking areas, educational and recreational facilities, administrative buildings, water storage and distribution infrastructure, market areas, storage facilities, and limited household gardening space. Where communal services are available outside the settlement, this requirement may be reduced to 30 m^2 per person, whereas enclosed accommodation units, such as tents or containers, should provide approximately 3.5–4.5 m^2 of covered living space per individual. To enhance fire safety and operational efficiency, dedicated areas should also be allocated for humanitarian organizations, including offices, warehouses, and staff facilities, while maintaining minimum separation distances of 2 m between individual shelters, 6 m between shelter clusters, and 15 m between block groups to reduce fire propagation risks (Sphere Project, 1997).

In this study, Kocaeli Province, Türkiye, was selected as the pilot study area due to its high seismic risk, dense population, and strategic industrial importance. Potential temporary shelter areas were identified through the integration of the Intuitionistic Fuzzy Analytic Hierarchy Process (IF-AHP) and GIS within a comprehensive multi-criteria decision-making (MCDM) framework. Unlike conventional site selection studies that primarily rely on classical Analytic Hierarchy Process (AHP) or fuzzy-based approaches, this research incorporates intuitionistic fuzzy theory to better represent the uncertainty and hesitation inherent in expert judgments, thereby improving the reliability and robustness of the decision-making process. Furthermore, the proposed GIS-based spatial analysis enables the simultaneous evaluation of multiple environmental, topographical, infrastructural, and accessibility criteria, resulting in a more realistic and practical suitability assessment for post-disaster temporary shelter planning. Consequently, the study provides a systematic and reproducible decision-support framework that can assist emergency management authorities in developing resilient disaster preparedness strategies and may serve as a transferable methodology for other earthquake-prone regions.

The remainder of this paper is organized as follows. Section 2 presents a comprehensive review of the existing literature on temporary shelter site selection, GIS-based spatial decision-making, and MCDM approach applied to disaster management. Section 3 describes the study area, data sources, evaluation criteria, and the proposed methodology, including the integration of IF-AHP and GIS for spatial suitability analysis. Section 4 presents and discusses the obtained suitability maps and analytical findings, highlighting the spatial distribution and prioritization of candidate temporary shelter areas. Finally, Section 5 summarizes the main findings of the study, discusses their practical implications for disaster risk reduction and emergency planning, addresses the limitations of the proposed framework, and provides recommendations for future research.

2. RELATED WORKS

Several studies have examined the evaluation and prioritization of temporary shelter areas through MCDM techniques. Omidvar et al. (2013) proposed an integrated GIS–MCDM framework for pre-earthquake temporary shelter site selection in Tehran, Iran. Their case study considered 13 criteria and 14 candidate shelter areas and applied TOPSIS, ELECTRE, SAW, and AHP methods. Although the study represents an important early contribution by comparing different MCDM techniques within a spatial decision-making context, the absence of an integrated aggregation procedure for combining the rankings obtained from different methods can be considered a methodological limitation. Nappi and Souza (2015) focused on structuring the criteria required for the selection and location of temporary shelters and proposed an AHP-based hierarchical evaluation framework. However, the study remained largely conceptual, as the criteria were not assessed through a practical decision-maker-based application. Soltani et al. (2015), using a Delphi panel, developed a comprehensive set of criteria for temporary shelter site selection after earthquakes. Their study is valuable in terms of criterion identification, since the final criteria were grouped under land suitability, socio-cultural considerations, service availability, and disaster risk reduction; nevertheless, it did not provide a spatial prioritization or ranking model for alternative shelter sites. Hosseini et al. (2016) applied AHP together with an integrated value model to support sustainable site selection for post-disaster temporary housing in urban areas. While the integrated value model strengthened the sustainability-oriented structure of the assessment, the use of a limited methodological framework indicates that the approach could be further improved through hybrid or uncertainty-based MCDM models.

Further methodological developments have also been observed in studies combining fuzzy logic, GIS, and MCDM tools. Trivedi and Singh (2017) proposed a hybrid group decision-support framework for emergency shelter area prioritization by determining criteria weights through fuzzy AHP and ranking candidate shelter locations using TOPSIS. Although this approach enhanced the treatment of expert uncertainty at the weighting stage, the ranking process was not fully embedded in a fuzzy environment, which may limit its ability to represent uncertainty throughout the whole decision process. Ömürgönülşen and Menten (2021) employed the fuzzy TOPSIS method to determine temporary shelter areas for Ankara Province; however, the absence of GIS integration can be regarded as a limitation, particularly because spatial suitability analysis is essential for shelter planning. Overall, the literature shows that existing studies have made substantial contributions to criterion identification, spatial evaluation, and MCDM-based prioritization. Nevertheless, there remains a need for more integrated frameworks that simultaneously incorporate spatial analysis, expert-based weighting, and uncertainty modelling. Güler et al. (2023) developed an integrated AHP–GIS approach for temporary shelter site selection in Kocaeli, Türkiye. Based on seven evaluation criteria, the proposed framework successfully identified suitable shelter locations and highlighted the effectiveness of combining GIS with MCDM techniques for disaster preparedness. Bitarafan and Daneshjoo (2023) evaluated alternative temporary housing solutions for post-disaster situations using the AHP. Considering criteria such as earthquake resistance, implementation speed, cost, construction complexity, and debris removal capability, the study identified the use of vernacular materials as the most suitable temporary housing option. Tuzkaya et al. (2024) proposed an integrated framework for temporary shelter site selection in Hatay following the 2023 Kahramanmaraş earthquakes. The study combined MCDM with the p-median mathematical model to evaluate settlement suitability and optimize the location of temporary shelter areas. Tarakçı (2026) applied the Fuzzy TOPSIS method to evaluate temporary shelter alternatives in İstanbul under potential earthquake scenarios. Based on ten evaluation criteria, the study identified the most suitable shelter locations and emphasized the importance of accessibility, proximity to affected populations, healthcare services, and environmental safety in post-disaster shelter planning.

3. MATERIALS AND METHODS

3.1. Data Set

The suitability assessment of temporary shelter areas in Kocaeli was performed using seven spatial evaluation criteria, namely slope (C1), faults (C2), streams (C3), buildings (C4), roads (C5), elevation (C6), and lithology (C7). These criteria were identified through a comprehensive review of previous studies, disaster management guidelines, and expert consultations, considering their direct influence on the safety, accessibility, and physical suitability of temporary shelter sites. Each criterion was processed as an independent GIS layer and standardized prior to the spatial suitability analysis.

GIS provide an effective spatial decision-support environment by integrating geospatial databases, analytical tools, computational techniques, and visualization capabilities to process and interpret location-based information. By combining spatial and attribute data within a unified platform, GIS enables comprehensive analyses that support complex planning and decision-making processes, particularly in disaster management applications (Shabani et al., 2024). In the present study, ArcMap 10.7 (ESRI Inc., Redlands, CA, USA) was employed to construct and analyze the spatial database used for temporary shelter site suitability assessment. The geospatial datasets representing the evaluation criteria were compiled from high-resolution satellite imagery together with official digital cartographic resources provided by Kocaeli Metropolitan Municipality. The database included 1:50,000-scale topographic maps, Digital Elevation Model (DEM) data, and other thematic spatial layers referenced to the WGS-84 datum and Universal Transverse Mercator (UTM) coordinate system. These datasets were converted into GIS-compatible formats and subjected to a comprehensive preprocessing procedure involving georeferencing, vector editing, raster conversion, and spatial standardization. To enable spatial multi-criteria analysis, each thematic layer was processed individually using ArcMap geoprocessing tools, including buffer generation, feature-to-raster conversion, raster reclassification, and weighted overlay analysis. The resulting standardized raster layers constituted the spatial database integrated with the IF-AHP for identifying the most suitable temporary shelter locations. This GIS-based database ensured spatial consistency among all evaluation criteria and provided a reliable framework for subsequent suitability analyses.

3.2. Intuitionistic Fuzzy AHP (IF-AHP)

Although the AHP is one of the most widely adopted weighting techniques in MCDM, its capability to represent uncertainty and hesitation in expert judgments is limited. To overcome this shortcoming, the IF-AHP extends the conventional AHP framework by incorporating intuitionistic fuzzy sets, which simultaneously consider membership, non-membership, and hesitation degrees. Consequently, the method provides a more realistic representation of experts' preferences under uncertain decision environments (Abdullah and Najib 2014).

Initially, the decision problem was structured hierarchically by defining the evaluation criteria. Experts subsequently performed pairwise comparisons using predefined linguistic expressions represented by triangular intuitionistic fuzzy (TIF) numbers (Table 1).

Table 1. Linguistic Terms and TIF numbers for IF-AHP (Karacan et al. 2020)

Linguistic Terms	**Preference Provision**	**(μ, v, π)**	**Reciprocals Preference Provision**	**Reciprocals (μ, v, π)**
Equally importance (EI)	1	(0.02, 0.18, 0.8)	1/1 (EI)	(0.02, 0.18, 0.8)
Intermediate Value (IV1)	2	(0.06, 0.23, 0.7)	1/2 (IV1')	(0.23, 0.06, 0.7)
Slightly more importance (SMI)	3	(0.13, 0.27, 0.6)	1/3 (SLI)	(0.27, 0.13, 0.6)
Intermediate Value (IV2)	4	(0.22, 0.28, 0.5)	1/4 (IV2')	(0.28, 0.22, 0.5)
High importance (HI)	5	(0.33, 0.27, 0.4)	1/5 (LI)	(0.27, 0.33, 0.4)
Intermediate Value (IV3)	6	(0.47, 0.23, 0.3)	1/6 (IV3')	(0.23, 0.47, 0.3)
Very high importance (VHI)	7	(0.62, 0.18, 0.2)	1/7 (VLI)	(0.18, 0.62, 0.2)
Intermediate Value (IV4)	8	(0.8, 0.1, 0.1)	1/8 (IV4')	(0.1, 0.8, 0.1)
Absolutely more importance (AMI)	9	(1, 0, 0)	1/9 (ALI)	(0, 1, 0)

Since multiple experts participated in the evaluation process, their relative contributions were quantified by calculating Decision Maker (DM) weights according to Eq. (1). The linguistic term-based on TIF numbers given in Table 2 should be used (Gocer and Sener, 2022).

$$\lambda_k = \frac{\mu_k + \pi_k(\frac{\mu_k}{\mu_k + v_k})}{\sum_{k=1}^{l}(\mu_k + \pi_k\left(\frac{\mu_k}{\mu_k + v_k}\right))},\ \sum_{k=1}^{l}\lambda_k = 1,\ k = (1,2, \dots l) \quad (1)$$

λ_k is the net weight value for the $k - th$ DM.

Table 2. The linguistic terms and IFSs for DMs' weights

Linguistic Terms	**IFSs** $(\boldsymbol{\mu(x), \nu(x), \pi(x)})$
Equally Important (EI)	(0.10, 0.80, 0.10)
Slightly Important (SI)	(0.25, 0.60, 0.15)
Fairly Important (FI)	(0.50, 0.40, 0.10)
Moderately Important (MI)	(0.75, 0.20, 0.05)
Very Important (VI)	(0.90, 0.05, 0.05)

Individual pairwise comparison matrices were then generated and converted into intuitionistic fuzzy matrices. To obtain a collective assessment, the individual intuitionistic fuzzy judgments were aggregated using the Intuitionistic Fuzzy Weighted Averaging (IFWA) operator proposed by Xu (2007), as expressed in Eq. (2).

$$r_{ij} = IFWA_\lambda\left(r_{ij}^{(1)}, r_{ij}^{(2)}, \dots, r_{ij}^{(l)}\right) = (\lambda_1 r_{ij}^{(1)} \oplus \lambda_2 r_{ij}^{(2)} \oplus \dots \oplus \lambda_l r_{ij}^{(l)}) \quad (2)$$

$$= \left[1 - \prod_{k=1}^{l}(1 - \mu_{ij}^{(k)})^{\lambda_k}, \prod_{k=1}^{l}(v_{ij}^{(k)})^{\lambda_k}, \prod_{k=1}^{l}(1 - \mu_{ij}^{(k)})^{\lambda_k} - \prod_{k=1}^{l}\left(v_{ij}^{(k)}\right)^{\lambda_k}\right]$$

Where,

$r_{ij} = (\mu_{ij}, v_{ij}, \pi_{ij})$;

$$\mu_{ij} = 1 - \prod_{k=1}^{l}(1 - \mu_{ij}^{(k)})^{\lambda_k}$$

$$v_{ij} = \prod_{k=1}^{l}(v_{ij}^{(k)})^{\lambda_k}$$

$$\pi_{ij} = \prod_{k=1}^{l}(1 - \mu_{ij}^{(k)})^{\lambda_k} - \prod_{k=1}^{l}\left(v_{ij}^{(k)}\right)^{\lambda_k}$$

The consistency of the aggregated comparison matrix was evaluated through the consistency ratio (CR) adapted for the IF-AHP framework (Eq. (3)).

$$CR = \frac{(\lambda_{max} - n)/n - 1}{RI} \tag{3}$$

Finally, the intuitionistic fuzzy weights were transformed into crisp values using the defuzzification procedure (Eq. (4)), and the normalized criteria weights (w_i) required for the GIS-based suitability analysis were calculated according to Eq. (5).

$$\bar{\bar{w}}i = \frac{\mu_i + \pi_i(\frac{\mu_i}{\mu_i + v_i})}{\sum_{i=1}^{n}(\mu_i + \pi_i\left(\frac{\mu_i}{\mu_i + v_i}\right))},\ \sum_{i=1}^{n}\bar{\bar{w}}i = 1,\ i = (1,2, \dots n) \tag{4}$$

$$w_i = \frac{\bar{\bar{w}}i}{\sum_{i=1}^{n}\bar{\bar{w}}i} \tag{5}$$

3.3. GIS-Based Spatial Analysis

The spatial analyses conducted in this study were performed using ArcMap 10.7, a widely adopted GIS platform for managing, processing, and analyzing spatial data. All datasets corresponding to the selected evaluation criteria were collected from official geospatial sources and converted into GIS-compatible thematic layers. Prior to the analysis, the datasets were standardized within the WGS-84/UTM coordinate system, georeferenced where necessary, and preprocessed to ensure spatial consistency (ESRI, 2024).

Each criterion layer was independently processed using the geoprocessing tools available in ArcMap, including buffer analysis, raster conversion, and raster reclassification, to produce standardized suitability maps. Subsequently, the criteria weights obtained from the IF-AHP were integrated into the GIS environment through the Weighted Overlay Analysis tool. By combining all weighted raster layers, a comprehensive spatial suitability map was generated, enabling the identification and prioritization of the most appropriate temporary shelter areas within the study region.

4. RESULTS

The IF-AHP pairwise comparisons were performed based on the opinions of an expert panel comprising five professionals with multidisciplinary expertise in disaster management. The DM group included two urban planners, one geophysical engineer, and two disaster management experts, each having over three years of professional experience in their respective disciplines. The multidisciplinary composition of the panel enhanced the reliability of the evaluation process by incorporating technical knowledge from urban planning, geosciences, and disaster management into the weighting of the assessment criteria. The collected expert judgments were subsequently aggregated to construct the intuitionistic fuzzy pairwise comparison matrices used in the IF-AHP analysis.

To reflect the multidisciplinary nature of the decision-making process, five DMs participated in the IF-AHP evaluation. The expert panel consisted of two urban planners, one geophysical engineer, and two disaster management specialists. Considering their professional qualifications and experience, the two urban planners were assigned the linguistic importance level of *Very Important (VI)*, whereas the geophysical engineer and the two disaster management specialists were evaluated as *Moderately Important (MI)* according to the linguistic scale presented in Table 2. Based on these assessments, the corresponding (DM) weights were computed using Eq. (1). The resulting normalized weights were 0.2350, 0.2350, 0.1767, 0.1767, and 0.1767, respectively.

Following the determination of the DMs' weights, each DM conducted pairwise comparisons of the evaluation criteria using the linguistic scale presented in Table 1. The judgments were expressed through intuitionistic fuzzy linguistic terms to capture the uncertainty and hesitation associated with subjective evaluations. The complete set of pairwise linguistic assessments provided by the five DMs is presented in Table 3. The linguistic judgments reported in Table 3 were subsequently transformed into their corresponding IFS numbers according to Table 1. Individual intuitionistic fuzzy comparison matrices were then established and aggregated using the IFWA operator defined in Eq. (2), resulting in the aggregated intuitionistic fuzzy comparison matrix presented in Table 4.

Table 3. Linguistic assessments of the criteria by DMs

	C1	C2	C3	C4	C5	C6	C7
C1	EI, EI, EI, EI, EI	SLI, LI, VLI, VLI, LI	LI, LI, VLI, LI, LI	EI, EI, LI, SMI, LI	LI, SLI, SLI, VLI, SLI	VLI, SLI, VLI, VLI, VLI	VLI, SLI, VLI, LI, VLI
C2	HI, HI, VHI, VHI, HI	EI, EI, EI, EI, EI	LI, SLI, LI, SMI, SLI	SMI, HI, SMI, HI, SMI	LI, HI, LI, SLI, LI	LI, HI, LI, SLI, LI	LI, HI, VLI, EI, VLI
C3	HI, VHI, VHI, HI, HI	HI, SMI, HI, SLI, SMI	EI, EI, EI, EI, EI	HI, HI, HI, LI, EI	SLI, HI, LI, VLI, LI	SLI, HI, SLI, VLI, LI	SLI, LI, SLI, SLI, LI
C4	SMI, EI, HI, SLI, HI	SLI, LI, SLI, LI, SLI	LI, LI, LI, HI, EI	EI, EI, EI, EI, EI	LI, SLI, EI, VLI, SLI	VLI, SLI, VLI, LI, VLI	LI, SLI, VLI, SLI, VLI
C5	HI, SMI, SMI, VHI, SMI	HI, LI, HI, SMI, HI	SMI, LI, HI, VHI, HI	HI, SMI, EI, VHI, SMI	EI, EI, EI, EI, EI	EI, SLI, LI, LI, LI	EI, SMI, VLI, VHI, SMI
C6	VHI, SMI ,VHI, VHI, VHI	HI, LI, HI, SMI, HI	SMI, LI, SMI, VHI, HI	VHI, SMI, VHI, HI, VHI	EI, SMI, HI, HI, HI	EI, EI, EI, EI, EI	SMI, SLI, HI, SMI, HI
C7	VHI, SMI, VHI, HI, VHI	HI, LI, VHI, EI, VHI	SMI, LI, HI, SMI, HI	HI, SMI, VHI, SMI,VHI	EI, SLI, VHI, VLI, SLI	SLI, SMI, LI, SLI, LI	EI, EI, EI, EI, EI

Table 4. Aggregation of pairwise comparison matrices via IFWA

IFWA	C1			C2			C3			C4			C5			C6			C7		
	μ	ν	π	μ	ν	π	μ	ν	π	μ	ν	π	μ	ν	π	μ	ν	π	μ	ν	π
C1	0.02	0.18	0.80	0.24	0.43	0.39	0.25	0.36	0.42	0.13	0.25	0.67	0.25	0.30	0.50	0.20	0.54	0.32	0.22	0.48	0.36
C2	0.46	0.24	0.33	0.02	0.18	0.80	0.24	0.25	0.52	0.22	0.27	0.52	0.28	0.28	0.45	0.28	0.28	0.45	0.21	0.41	0.47
C3	0.48	0.23	0.32	0.25	0.24	0.52	0.02	0.18	0.80	0.28	0.27	0.48	0.27	0.35	0.42	0.27	0.32	0.47	0.28	0.23	0.50
C4	0.21	0.22	0.61	0.27	0.22	0.52	0.25	0.30	0.48	0.02	0.18	0.80	0.21	0.31	0.56	0.22	0.48	0.36	0.24	0.38	0.45
C5	0.30	0.25	0.50	0.28	0.28	0.45	0.35	0.27	0.42	0.29	0.24	0.56	0.02	0.18	0.80	0.22	0.25	0.58	0.25	0.32	0.55
C6	0.54	0.20	0.32	0.28	0.28	0.45	0.32	0.27	0.47	0.48	0.22	0.36	0.22	0.25	0.58	0.02	0.18	0.80	0.23	0.24	0.54
C7	0.48	0.22	0.36	0.39	0.24	0.47	0.23	0.28	0.50	0.38	0.24	0.45	0.30	0.28	0.55	0.24	0.23	0.54	0.02	0.18	0.80

Based on the aggregated intuitionistic fuzzy comparison matrix, the intuitionistic fuzzy weights of the evaluation criteria were calculated. The obtained fuzzy weights were defuzzified using Eq. (4) and subsequently normalized according to Eq. (5) to obtain the final IF-AHP criteria weights. The resulting normalized weights are reported in Table 5.

Table 5. Weights of criteria via IF-AHP

Criteria no	**Intutionistic Fuzzy Weights**			**Defuzzified Weights**	**Normalized Weights**	**Rank**
	μ	**ν**	**π**			
C1	0.1885	0.3014	0.5100	0.2592	0,1142	**7**
C2	0.2509	0.2491	0.5000	0.3216	0,1429	**4**
C3	0.2740	0.2322	0.4937	0.3447	0,1502	**3**
C4	0.2031	0.2414	0.5554	0.2730	0,1204	**6**
C5	0.2499	0.2408	0.5093	0.3206	0,1396	**5**
C6	0.3181	0.2275	0.4543	0.3883	0,1691	**1**
C7	0.3049	0.2202	0.4747	0.3755	0,1636	**2**

The normalized IF-AHP weights presented in Table 5 indicate that the evaluation criteria exhibit different levels of influence on temporary shelter site suitability. The criterion with the highest priority was C6 (Elevation), whereas C1 (Slope) received the lowest importance weight. Accordingly, the relative importance of the criteria was ranked as follows: C6 > C7 > C3 > C2 > C5 > C4 > C1. These findings suggest that topographical and geological characteristics have a greater impact on the selection of suitable temporary shelter locations than the remaining evaluation criteria within the proposed decision-making framework.

Following the reclassification of all thematic layers into a common suitability scale, the spatial integration process was carried out using the Weighted Overlay tool available in the ArcMap 10.7 Spatial Analyst extension. In this study, the Weighted Sum approach was adopted to combine the standardized raster layers. During this procedure, the suitability values of each criterion were multiplied by their corresponding normalized IF-AHP weights, and the weighted raster layers were subsequently aggregated to generate a composite suitability index. The resulting raster surface represents the cumulative influence of all evaluation criteria and forms the basis for identifying the most suitable temporary shelter locations within the study area.

To ensure a consistent interpretation of the spatial analysis results, all raster layers were classified into a five-level suitability scale. Suitability scores ranged from 1 (highly unsuitable) to 5 (very suitable), where higher values indicate increasingly favorable conditions for temporary shelter site selection. This classification approach has been widely adopted in previous GIS-based land suitability studies (Şentürk and Erener, 2017; Kumlu and Tüdeş, 2019; Ofluoğlu, 2023).

Following the completion of the raster processing and weighted overlay analyses, the Weighted Sum method produced the final spatial suitability map shown in Figure 1. The generated map illustrates the distribution of potential temporary shelter areas across Kocaeli Province based on the combined influence of the selected evaluation criteria. Suitability scores range from 1 (highly unsuitable) to 5 (very suitable), where higher values indicate locations that better satisfy the physical, geological, and accessibility requirements for temporary shelter establishment.

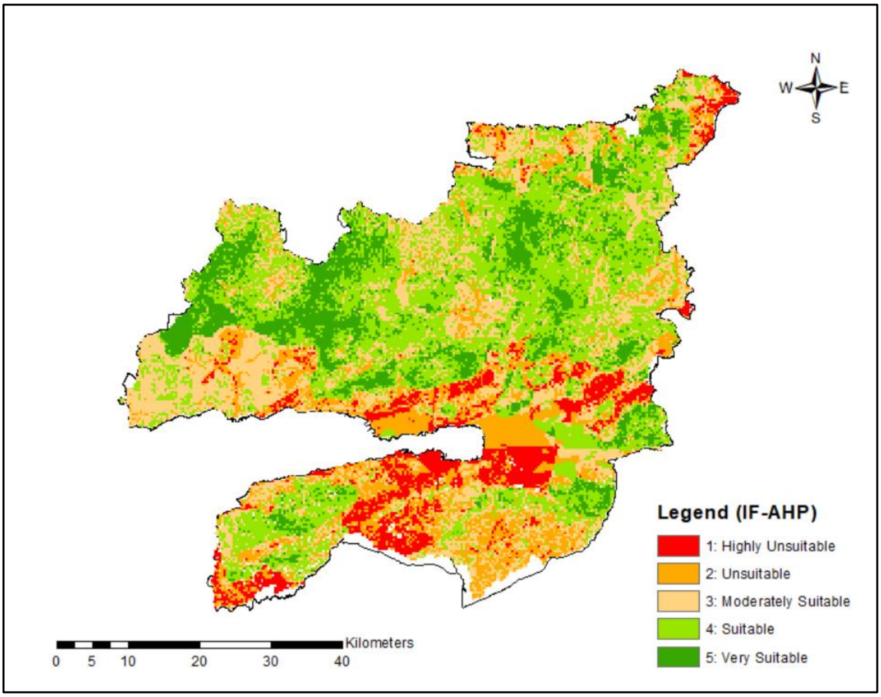

Figure 1. Temporary Shelter Areas for Kocaeli

The spatial distribution of these suitability classes provides a comprehensive basis for identifying priority locations that can support emergency shelter planning and post-disaster response activities.

5. DISCUSSION AND CONCLUSION

The selection of temporary shelter areas represents one of the most critical decisions during the disaster preparedness and response phases, as inappropriate site selection may increase the vulnerability of affected populations and reduce the effectiveness of humanitarian operations. In this study, an integrated IF-AHP and GIS framework was proposed to identify suitable temporary shelter locations for Kocaeli Province, one of the most earthquake-prone and industrialized regions of Türkiye. Compared with conventional AHP-based approaches, the proposed methodology explicitly incorporates the hesitation and uncertainty associated with expert judgments, thereby providing a more reliable weighting structure for spatial decision-making.

The IF-AHP results revealed that elevation (C6) and lithology (C7) were the two most influential criteria in determining the suitability of temporary shelter areas, whereas slope (C1) received the lowest priority. This finding highlights the dominant role of topographical and geological characteristics in post-disaster shelter planning.

Locations with favorable elevation and stable geological formations are generally less susceptible to secondary hazards such as flooding, liquefaction, and ground instability, making them more suitable for emergency settlements. Although accessibility-related criteria such as roads and buildings also contributed to the evaluation, they exhibited relatively lower importance than the physical characteristics of the terrain, indicating that site safety remains the primary consideration in shelter planning.

The suitability map generated through the integration of IF-AHP and GIS provides a spatially explicit representation of potential temporary shelter areas across Kocaeli Province. By combining standardized thematic layers with intuitionistic fuzzy criteria weights using the Weighted Sum approach, the proposed framework enables decision-makers to evaluate multiple spatial factors simultaneously while accounting for uncertainty in expert assessments. Compared with previous studies, which predominantly employed classical AHP or conventional fuzzy methods, the present study extends the existing literature by integrating intuitionistic fuzzy theory into GIS-based spatial suitability analysis, thereby enhancing the robustness and credibility of the decision-making process. From a practical perspective, the proposed methodology can support AFAD, local municipalities, and urban planning authorities in developing disaster preparedness strategies and identifying priority areas for temporary shelter establishment before the occurrence of major earthquakes. Furthermore, the resulting suitability maps may contribute to evacuation planning, emergency logistics, and land-use management by providing a scientific basis for strategic decision-making.

Despite these contributions, several limitations should be acknowledged. The proposed framework was developed using seven evaluation criteria and was applied only to Kocaeli Province. Future studies may incorporate additional environmental, socio-economic, and infrastructure-related criteria, as well as alternative MCDM techniques such as ANP, DEMATEL, or PROMETHEE to further investigate the robustness of the obtained results. In addition, integrating real-time spatial data, remote sensing technologies, and dynamic disaster scenarios could further improve the applicability of temporary shelter planning under changing post-disaster conditions.

ACKNOWLEDGMENT

This work has been supported by Kocaeli University Scientific Research Projects Coordination Unit undergrant number #FBA-2022-3100.

REFERENCES

Abdullah, L., Najib, L. A. (2014). A new preference scale of intuitionistic fuzzy analytic hierarchy process in multi-criteria decision making problems. J. Intell. Fuzzy Syst., 26, 1039–1049.

AFAD. (2014). T.C. Başbakanlık Afet ve Acil Durum Yönetimi Başkanlığı Türkiye Afet Müdahale Planı, https://www.afad.gov.tr/kurumlar/afad.gov.tr/2419/files/Afet_Mud_Pl_ResmiG_2 0122013.pdf

Bitarafan, A., & Daneshjoo, K. (2023). Evaluating the Various Methods of Temporary Shelter in Crisis Situations Using the AHP Method. Safe City, 5(4), 21-37.

ESRI, (2024). ArcGIS, Access: https://www.esri.com/en-us/home

Gocer, F., & Sener, N. (2022). Spherical fuzzy extension of AHP-ARAS methods integrated with modified k-means clustering for logistics hub location problem. Expert Systems, 39(2), e12886.

Güler, E., Azkeskin, S. A., & Aladağ, Z. (2023). Determination of Temporary Accommodation Areas in Earthquake via MCDM and GIS.

Hosseini Sabzevari, S. A., Mottaki, Z., Hassani, A., Zandiyeh, S., Aslani, F. (2022). Temporary Housing Site Selection in Soffeh Mountain, District 5 of Isfahan, Iran. International Journal of Disaster Resilience in the Built Environment, 14(5), 611-627.

İsmail, İ. (2021). An Optimization Model to Control the Flow of Relief Commodities in Humanitarian Supply Chain Under Uncertainty, Doktora Tezi, İstanbul Teknik Üniversitesi, Fen Bilimleri Enstitüsü, İstanbul, 692574.

Kara, B. Y., Savaşer, S. (2017). Humanitarian Logistics. In Leading Developments from INFORMS Communities. INFORMS, 263-303.

Karacan, I., Senvar, O., Arslan, O., Ekmekçi, Y., & Bulkan, S. (2020). A novel approach integrating intuitionistic fuzzy analytical hierarchy process and goal programming for chickpea cultivar selection under stress conditions. Processes, 8(10), 1288.

Kumlu, K.B.Y., Tüdeş S. (2019). Determination of Earthquake-Risky Areas in Yalova City Center (Marmara Region, Turkey) using GIS-Based Multicriteria Decision-Making Techniques (Analytical Hierarchy Process and Technique for Order Preference by Similarity to Ideal Solution). Natural Hazards, 96, 999−1018.

Nappi, M. M. L., Souza, J. C. (2015). Disaster Management: Hierarchical Structuring Criteria for Selection and Location of Temporary Shelters. Natural Hazards, 75, 2421-2436.

Ofluoğlu, A. (2023). Geçici Barınma Merkezi Yer Seçimi İçin Bütünleşik Bir Yaklaşım: Trabzon İli Örneği. Doktora Tezi, Karadeniz Teknik Üniversitesi, Sosyal Bilimler Enstitüsü. Trabzon. 834400.

Omidvar, B., Baradaran-Shoraka, M., Nojavan, M. (2013). Temporary Site Selection and Decision-Making Methods: A Case Study of Tehran, Iran, Disasters, 37(3), 536-553.

Ömürgönülşen, M., Menten, C. (2021). Bulanık TOPSIS Yöntemi ile Ankara İli İçin Olası Afet Sonrası Geçici Barınma Alanlarının Seçimi, Doğal Afetler ve Çevre Dergisi, 7(1), 159-175.

Schiffling, S., Hannibal, C., Tickle, M., Fan, Y. (2022). The Implications of Complexity for Humanitarian Logistics: A Complex Adaptive Systems Perspective. Annals of Operations Research, 319(1), 1379-1410.

Shabani, T., Defe, R., Mavugara, R., Mupepi, O., & Shabani, T. (2024). Application of Geographic Information Systems (GIS) and Remote Sensing (RS) in solid waste management in Southern Africa: a review. SN Social Sciences, 4(2), 39.

Soltani, A., Ardalan, A., Boloorani, A. D., Haghdoost, A., Hosseinzadeh-Attar, M. J. (2015). Criteria for Site Selection of Temporary Shelters After Earthquakes: A Delphi Panel. PLoS currents, 7, 1-10.

Sphere Projesi, (1997). https://spherestandards.org/wpcontent/uploads/2018/06/The_Sphere_Handbook_2011_Turkish.pdf

Şentürk, E., Erener, A. (2017). Determination of Temporary Shelter Areas in Natural Disasters by GIS: A Case Study, Gölcük/Turkey. International Journal of Engineering and Geosciences, 2(3), 84-90.

Tarakçı, B. İ. (2026). Fuzzy TOPSIS-Based Multi-Criteria Evaluation Model for Post-Disaster Temporary Shelter Site Selection: The Case of İstanbul, Civil Engineering and Architecture, 14(3A): 2578-2596.

Trivedi, A., Singh, A. (2017). Prioritizing Emergency Shelter Areas using Hybrid Multi-Criteria Decision Approach: A Case Study. Journal of Multi-Criteria Decision Analysis, 24(3-4), 133-145.

Tuzkaya, U. R., Alp, S., Aydın, N., Şeker, Ş., & Geçici, E. (2025). Determination and Evaluation of Alternatives for Post-Earthquake Temporary Sheltering Area. Journal of Transportation and Logistics, 10(2), 256-295.

Xu, Z.S. (2007). Intuitionistic Fuzzy Aggregation Operators, IEEE Transactions on Fuzzy Systems, 15, 1179–1187.

Chapter 3

The Integration of Artificial Intelligence and Building Informatıon Modeling (BIM) in Green Building Certification Processes in the Literature

Mehmet UZUN[1]

Abstract

Sustainable and environmentally friendly building design has become one of the construction industry's most critical responsibilities in the fight against the global climate crisis. Green building certification systems such as LEED, BREEAM, DGNB, and EDGE verify the environmental performance of buildings using objective criteria. However, traditional certification processes cannot be optimized due to intensive data tracking, high costs, time-consuming manual calculations, and static evaluations conducted after the design phase. This study is a comprehensive literature review examining the automation, optimization, and transformation of green building certification processes into decision-support mechanisms through the integration of Building Information Modeling (BIM) and Artificial Intelligence (AI) technologies. By screening high-quality academic studies published in the Scopus, Web of Science, and Google Scholar databases over the past 10 years, BIM-based energy analysis tools, AI-supported life cycle assessment (LCA), carbon footprint estimation using machine learning algorithms, and certification credit automation models were categorized. The findings demonstrate that the synergy between BIM and AI reduces data processing times in certification processes by up to 70% and paves the way for optimized engineering solutions by providing real-time performance feedback during the design phase.

Keywords: Green Buildings, LEED, Building Information Modeling (BIM), Artificial Intelligence, Machine Learning, Life Cycle Assessment.

[1] Doç. Dr., ORCID: 0000-0002-6347-1243
mehmetuzun@kmu.edu.tr, Karamanoğlu Mehmetbey Üniversitesi, Mühendislik Fakültesi, İnşaat Mühendisliği Bölümü, Karaman, Türkiye

Literatürde Yeşil Bina Sertifikasyon Süreçlerinde Yapay Zekâ Ve Yapı Bilgi Modellemesi (Bım) Entegrasyonu

Özet

Sürdürülebilir ve çevre dostu yapı tasarımı, küresel iklim kriziyle mücadelede inşaat sektörünün en kritik sorumluluklarından biri haline gelmiştir. LEED, BREEAM, DGNB ve EDGE gibi yeşil bina sertifikasyon sistemleri, yapıların çevresel performanslarını objektif kriterlerle tescil etmektedir. Ancak geleneksel sertifikasyon süreçleri; yoğun veri takibi, yüksek maliyet, zaman alıcı manuel hesaplamalar ve tasarım aşamasından sonra gerçekleştirilen statik değerlendirmeler nedeniyle optimize edilememektedir. Bu çalışma, Yapı Bilgi Modellemesi (BIM) ve Yapay Zekâ (AI) teknolojilerinin entegrasyonu ile yeşil bina sertifikasyon süreçlerinin otomasyonu, optimizasyonu ve karar destek mekanizmalarına dönüştürülmesini inceleyen kapsamlı bir literatür özetidir. Son 10 yılda Scopus, Web of Science ve Google Scholar veri tabanlarında yayınlanan nitelikli akademik çalışmalar taranarak; BIM tabanlı enerji analizi araçları, AI destekli yaşam döngüsü değerlendirmesi (LCA), makine öğrenmesi algoritmalarıyla karbon ayak izi tahmini ve sertifika kredi otomasyon modelleri tasnif edilmiştir. Bulgular, BIM ve AI sinerjisinin sertifikasyon süreçlerindeki veri işleme sürelerini %70'e varan oranlarda azalttığını, tasarım aşamasında anlık performans geri bildirimleri sağlayarak optimize edilmiş mühendislik çözümlerine zemin hazırladığını göstermektedir.

Anahtar Kelimeler: Yeşil Binalar, LEED, Yapı Bilgi Modellemesi (BIM), Yapay Zekâ, Makine Öğrenmesi, Yaşam Döngüsü Değerlendirmesi.

1. INTRODUCTION

The construction sector is responsible for approximately 36% of primary energy consumption and 40% of energy-related carbon dioxide (CO_2) emissions globally [1]. In order to mitigate the effects of global warming and achieve sustainable development goals, the concept of "green buildings"—which aims to minimize the environmental impact of structures—has gained significant importance over the past twenty years. Green buildings are structures designed, constructed, and operated in accordance with criteria such as energy efficiency, water conservation, sustainable material selection, indoor environmental quality, and land use [2].

Various green building certification systems have been developed worldwide to standardize and document the environmental impact of these structures. The most widely recognized of these systems are LEED (Leadership in Energy and Environmental Design), which originated in the United States; BREEAM (Building Research Establishment Environmental Assessment Method), which originated in the United Kingdom; and DGNB (Deutsche Gesellschaft für Nachhaltiges Bauen), which originated in Germany [3]. Although certification processes transparently demonstrate a building's sustainability performance, they are bureaucratic, data-intensive, costly, and prone to errors. In traditional methods, the link between design data and certification criteria is established manually, which prevents designers from seeing the environmental impacts of immediate changes [4].

Building Information Modeling (BIM), a pioneer of digital transformation in the worlds of engineering and architecture, has the potential to fill this data gap by providing a digital representation of a building's physical and functional characteristics [5]. BIM incorporates not only geometric data but also rich metadata such as material properties, thermal transmittance coefficients, and acoustic values [6]. However, BIM alone may prove insufficient for complex and nonlinear design optimizations. This is precisely where Artificial Intelligence (AI) and Machine Learning (ML) algorithms come into play [7]. With its capabilities for processing large datasets, pattern recognition, and high-accuracy forecasting, AI transforms the static database provided by BIM into a dynamic decision-support system.

The purpose of this study is to conduct a comprehensive review of the current literature on the integration of BIM and Artificial Intelligence in the automation and optimization of green building certification processes, to classify the methodologies employed, to identify existing technological bottlenecks, and to shed light on future research directions.

2. BUILDING INFORMATION MODELING (BIM) AND ITS ROLE IN GREEN BUILDING ASSESSMENT

Traditional green building certification is based on the principle of submitting hundreds of documents, reports, and invoices—collected after the project's completion or during the final stages of design—to the certification board [3]. This static approach makes it difficult for architects and engineers to optimize their design decisions in the early stages.

The key limitations and bottlenecks faced by traditional processes can be summarized as follows [4,8,9]:

- **Data Discontinuity:** The use of different software to produce architectural, structural, and mechanical designs results in the manual re-entry of data required for sustainability analyses, which increases the risk of data loss and errors.
- **Time and Cost Overruns:** Repeating analyses such as energy simulations, daylighting analyses, and Life Cycle Assessments (LCA) with every design revision leads to significant time loss and a multiplication of expert consulting costs.
- **Late Performance Feedback:** Decisions that need to be resolved during the early design phase—such as a building's thermal mass or orientation—become impossible to change because certification consultants provide analysis results too late.

Given the challenges and time losses encountered in traditional green building certification processes, there has been a search for new methods. One of the key approaches proposed to address these issues is the use of Building Information Modeling (BIM) in green building assessments.

Building Information Modeling (BIM) is not merely a three-dimensional (3D) visualization and drafting tool, but rather an object-based information platform that manages the geometric and semantic data required throughout a building's entire life cycle, from the conceptual phase to demolition [10]. The effectiveness of BIM in green building assessment and certification processes is directly related to the model's Level of Development (LOD). While massing models at the LOD 100–200 level are sufficient for basic energy simulations during the early design phase, the certification application and construction phases require detailed models at the LOD 300–400 level that include materials' thermal conductivity coefficients, renewable content ratios, and manufacturer data [11,12].

The success of BIM-supported green building projects depends on the seamless transfer of data throughout the building's entire life cycle. The "Life Cycle Diagram for BIM-Supported Green Building Projects" presented in Figure

1 illustrates, step by step, how this integration works from the feasibility stage through to demolition.

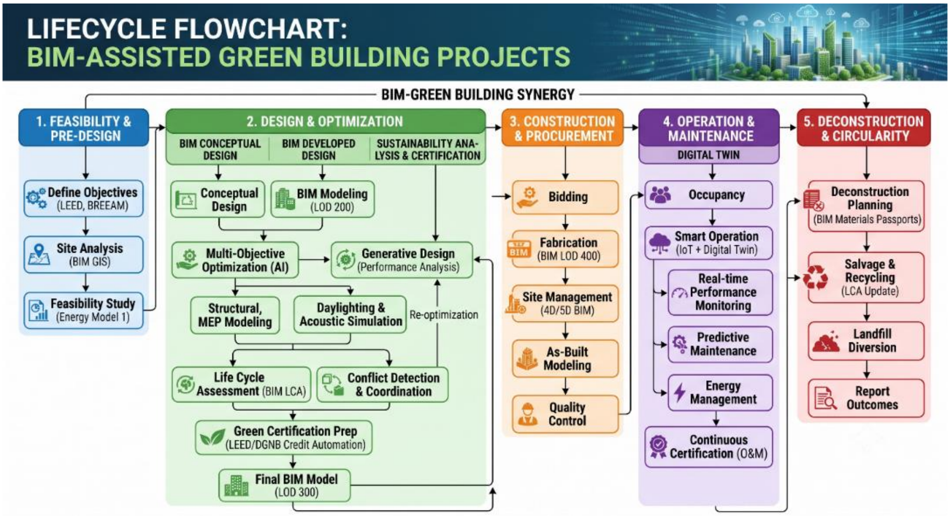

Figure 1. The Life cycle of BIM-supported green building projects

As shown in Figure 1, during the “Design and Optimization” phase—the second stage of the life cycle—BIM serves as the primary data source for Building Energy Modeling (BEM), Dynamic Life Cycle Assessment (LCA), and certification automation. Open data standards such as Industry Foundation Classes (IFC) and Green Building XML (gbXML) play a critical role in transferring BIM data to sustainability software [5]. While gbXML specifically facilitates the transfer of thermal zoning and geometric surface data to energy simulation tools, IFC carries the building’s semantic data across all disciplines.

The basic linear energy transfer equation used to calculate the energy performance index of buildings is as follows [3]:

$$Q = U \times A \times \Delta T$$

Here, Q represents the amount of heat transfer (watts), U represents the material’s total thermal transmittance (W/m²K), A represents the surface area (m²), and ΔT represents the temperature difference between the interior and exterior environments (°C). BIM eliminates the burden of traditional calculations by automatically providing the A parameter based on geometric objects and the U parameter based on material properties [3].

However, in the fourth and fifth phases highlighted in Figure 1 (Operation and Deconstruction), BIM manages not only the design but the entire future of the building. During the Operation phase, "Digital Twins" powered by IoT sensors provide continuous performance verification; at the end of the structure's service life, "Material Passports" within the BIM model enable the dismantling, recycling, and integration of building components into the circular economy [13].

3. INTEGRATION OF ARTIFICIAL INTELLIGENCE AND MACHINE LEARNING INTO PROCESSES

Although BIM is effective at providing data to architects, selecting the optimal "green" solution from among thousands of alternative design combinations is an optimization problem that exceeds human capabilities [5]. Artificial Intelligence (AI) steps in at this point to handle the processes of optimization, forecasting, and pattern recognition.

Among the most commonly used artificial intelligence methods in the literature are Artificial Neural Networks (ANN), Support Vector Machines (SVM), Random Forest, and Genetic Algorithms (GA) [7]. Genetic algorithms are used specifically in multi-objective optimization problems to both minimize initial investment costs and maximize the LEED energy score [5]. The application areas of these methods used in green building analyses, along with the input parameters obtained from BIM and their accuracy levels, are presented in Table 1.

Table 1: Artificial intelligence algorithms used in green building analyses

Artificial Intelligence Method	Scope of Application	Input Parameters (Retrieved from BIM)	Coefficient of Determination (R^2)
Artificial Neural Networks (ANN) [7]	Energy Consumption Estimate	Wall U-Value, Window-to-Wall Ratio, Orientation	0.94 - 0.98
Random Forest (RF) [7]	Carbon Footprint and LCA	Concrete Grade, Steel Quantity, Floor Area	0.89 - 0.93
Genetic Algorithms [5]	Design Optimization	All Building Geometry Variations	High Optimization Success

In the training of machine learning models, BIM data from past projects and actual energy bills are used as input [7]. To minimize the error rate during the training process, the formula for the mean squared error (MSE) function used in artificial neural networks is as follows [7]:

$$MSE = (1 / n) \times \Sigma (yi - \hat{y}i)^2$$

The term n in the formula represents the total number of data points or observations used during the model training and testing processes. The parameter yi denotes the measured actual data value (e.g., actual annual energy consumption or emission levels) obtained for the relevant building via sensors or actual utility bills, while the parameter $\hat{y}i$ represents the predicted value calculated by the trained machine learning or artificial intelligence model using BIM data. Calculating the square of the difference between the actual value and the predicted value ($yi - \hat{y}i$) prevents negative and positive deviations from canceling each other out while ensuring that large-scale errors are reflected in the model as higher penalty scores; furthermore, when the ***MSE*** value—obtained by dividing the sum of these differences by the number of observations—approaches zero, it indicates that the model's prediction accuracy is at its maximum level [7].

4. APPLICATIONS OF BIM AND AI INTEGRATION IN CERTIFICATION AUTOMATION

Some of the credits required to obtain LEED or BREEAM certification are entirely dependent on geometric and locational criteria [3]. For example, criteria such as proximity to public transportation or daylighting ratios under the indoor environmental quality category can be automatically scored without the need for manual intervention by integrating the BIM model with GIS (Geographic Information Systems) data and scanning it using rule-based artificial intelligence engines [10]. In addition to design optimization, while traditional LCA analyses are typically conducted after the design is complete, thereby precluding the possibility of retroactive changes [14], the real-time linking of quantity takeoff lists in the BIM model to environmental databases via artificial intelligence algorithms makes this process dynamic. Thanks to this integration, a change made by the designer to the size or material type of a reinforced concrete column in the model can instantly update the global warming potential (GWP) that the building will generate over its 50-year lifespan through real-time graphs [14]. Since certification processes are not limited to the design phase but also cover the building's actual performance after it is put into operation, real-time temperature, humidity, and CO_2 data from Internet of Things (IoT) sensors are transferred to the BIM model to create the building's

"Digital Twin" [7]. The deep learning algorithms incorporated into the process continuously monitor this data to detect anomalies in energy consumption in advance and ensure that the achieved certification performance score is maintained throughout the building's lifespan [7].

5. CONCLUSION AND EVALUATION

This literature review provides a detailed analysis of the construction industry's digital transformation process in light of the global climate crisis and energy goals, highlighting the transformative impact of Building Information Modeling (BIM) and Artificial Intelligence (AI) integration on green building certification systems. The findings demonstrate that chronic bottlenecks inherent in traditional certification processes—such as the heavy manual workload, high consulting costs, interdisciplinary data losses, and static performance evaluations conducted long after the design phase—can be overcome through AI-enabled BIM architectures.

When evaluated in terms of process automation, rule-based artificial intelligence engines that scan geographic, geometric, and semantic data in BIM models reduce data processing times in credit assessment and scoring processes by up to 70%. In addition, the integration of predictive algorithms such as machine learning and artificial neural networks (ANNs) reduces the analysis time required by traditional, computationally intensive simulation software (such as EnergyPlus) from hours to seconds. Meanwhile, multi-criteria optimization models supported by genetic algorithms (NSGA-II) instantly balance conflicting parameters—such as building material selection, orientation, window-to-wall ratios, and initial investment costs—thereby providing designers with optimal "green" solutions at a very early stage.

Furthermore, the process is evolving to encompass the entire life cycle of a building, rather than being limited to just the design or construction phases. Thanks to BIM-based Dynamic Life Cycle Assessment (LCA), the impact of an instantaneous material change made during the design phase on the building's 50-year embedded carbon footprint can be dynamically tracked. During the operational phase, "Digital Twins"—created by integrating Internet of Things (IoT) sensor data into the BIM environment—monitor the building's actual performance, ensuring that its green building certification is maintained throughout its lifespan.

Despite all this potential, interoperability constraints in data transfers between software systems, the "black box" nature of advanced deep learning models—which lack transparency—and the industry's reluctance to share data are the primary obstacles to full automation. In the future, with the advancement of

Explainable Artificial Intelligence (XAI) approaches, the automatic review of building codes by Large Language Models (LLMs), and the widespread adoption of blockchain-based transparent certification tracking mechanisms, it is anticipated that the concept of green building consulting will largely be replaced by AI-powered integrated decision support systems. To ensure that the engineering and architecture communities can derive maximum benefit from this synergy, it is critical to support open-source data standards and establish interdisciplinary data-sharing ecosystems.

REFERENCES

[1] Energy U. Buildings energy data book. United States Am Energy Effic Renew Energy 2011.

[2] Jalaei F, Jrade A. Integrating building information modeling (BIM) and LEED system at the conceptual design stage of sustainable buildings. Sustain Cities Soc 2015;18:95–107. https://doi.org/10.1016/j.scs.2015.06.007.

[3] Azhar S, Carlton WA, Olsen D, Ahmad I. Building information modeling for sustainable design and LEED® rating analysis. Autom Constr 2011;20:217–24. https://doi.org/10.1016/j.autcon.2010.09.019.

[4] Schlueter A, Thesseling F. Building information model based energy/exergy performance assessment in early design stages. Autom Constr 2009;18:153–63. https://doi.org/10.1016/j.autcon.2008.07.003.

[5] Rahmani Asl M, Zarrinmehr S, Bergin M, Yan W. BPOpt: A framework for BIM-based performance optimization. Energy Build 2015;108:401–12. https://doi.org/10.1016/j.enbuild.2015.09.011.

[6] Eastman CM. Building product models: computer environments, supporting design and construction. CRC press; 2018.

[7] Abioye SO, Oyedele LO, Akanbi L, Ajayi A, Davila Delgado JM, Bilal M, et al. Artificial intelligence in the construction industry: A review of present status, opportunities and future challenges. J Build Eng 2021;44:103299. https://doi.org/10.1016/j.jobe.2021.103299.

[8] Azhar S, Brown JW, Sattineni A. A case study of building performance analyses using building information modeling. Editor no identificado; 2014.

[9] Autodesk I. Improving building industry results through integrated project delivery and building information modeling. White Pap 2008.

[10] Lu Y, Wu Z, Chang R, Li Y. Building Information Modeling (BIM) for green buildings: A critical review and future directions. Autom Constr 2017;83:134–48. https://doi.org/10.1016/j.autcon.2017.08.024.

[11] Volk R, Stengel J, Schultmann F. Building Information Modeling (BIM) for existing buildings — Literature review and future needs. Autom Constr 2014;38:109–27. https://doi.org/10.1016/j.autcon.2013.10.023.

[12] Pehlivan CN, Forgó N, Valcke P. The EU artificial intelligence (AI) act: A commentary. Kluwer Law International BV; 2024.

[13] GhaffarianHoseini A, Zhang T, Nwadigo O, GhaffarianHoseini A, Naismith N, Tookey J, et al. Application of nD BIM Integrated Knowledge-based Building Management System (BIM-IKBMS) for inspecting post-construction energy efficiency. Renew Sustain Energy Rev

2017;72:935–49. https://doi.org/10.1016/j.rser.2016.12.061.
[14] Soust-Verdaguer B, Llatas C, García-Martínez A. Critical review of bim-based LCA method to buildings. Energy Build 2017;136:110–20. https://doi.org/10.1016/j.enbuild.2016.12.009.

Chapter 4

Polymer-Based Part Production with FDM Technology: Fundamental Principles, Materials, and the Effects of Production Parameters

Semih DURAN[1]

Abstract

Fused Deposition Modeling (FDM) is one of the most widely used additive manufacturing techniques for producing polymer-based parts from thermoplastic filaments. In this method, a filament material is heated to a semi-molten state, extruded through a nozzle, and deposited layer by layer according to the toolpaths generated from a digital model. One of the main advantages of FDM is that it offers a low-cost, accessible, and flexible production route for rapid prototyping, customized parts, educational applications, and small-scale functional components. Moreover, its compatibility with a wide range of polymer-based materials, including PLA, ABS, PETG, TPU, PA, and reinforced or composite filaments, makes FDM an attractive manufacturing method for different engineering applications.

In recent years, the development of printer systems, slicing software, filament materials, and process control strategies has further increased the use of FDM in both academic research and industrial practice. However, the performance of FDM-printed parts is strongly influenced by material properties and process parameters. Parameters such as layer thickness, infill density, infill pattern, raster angle, build orientation, nozzle temperature, bed temperature, printing speed, and cooling conditions directly affect interlayer bonding, void formation, surface quality, dimensional accuracy, and mechanical behavior. In addition, material characteristics such as viscosity, thermal stability, shrinkage tendency, moisture sensitivity, and interlayer bonding capability play an important role in printability and final part performance. This study presents a comprehensive overview of FDM technology, highlighting its fundamental principles, polymer-based materials, material selection criteria, and the effects of production parameters on part performance. It aims to provide researchers, engineers, and practitioners with a clear understanding of FDM as a practical and versatile additive manufacturing method for polymer-based part production.

Keywords: FDM, filaments, production parameters

[1] Asst. Prof., Kafkas University, Faculty of Engineering and Architecture, Department of Mechanical Engineering, semih.duran@kafkas.edu.tr, ORCID: 0000-0001-7107-1461

1. Introduction

The development of additive manufacturing technology dates back to the 1980s. Initially used for rapid prototyping, these technologies have gradually expanded into a broader engineering field with the increase in material diversity, the development of printer systems, the strengthening of software infrastructure, and the improvement of process control capabilities. While resin-based systems and conceptual model production were more prominent in the early stages, today it has become possible to produce parts using polymers, metals, ceramics, composites, and recycled materials. This development has made it necessary to evaluate additive manufacturing not only as a manufacturing technique but also in terms of materials engineering, design optimization, sustainable production, and the digital manufacturing chain (Chapiro, 2016; De Leon et al., 2016; Patti et al., 2022).

Additive manufacturing is an advanced production technology based on the fabrication of parts, generally layer by layer, from three-dimensional model data, and in this respect, it differs from conventional manufacturing methods based on machining or forming. Since the part is obtained by the controlled addition of material in this method, the production process should be considered not only as a geometrical shaping operation but also as a holistic manufacturing approach in which the relationship between design, material selection, process parameters, and final performance is managed together. In conventional manufacturing methods, parts are often obtained by removing material from the starting stock, molding, or plastic forming, whereas in additive manufacturing, the transition from the digital model to the physical product takes place directly through a layered structure. This makes additive manufacturing a strong option, particularly for the production of parts with complex geometries, customized designs, low production volumes, or rapid prototyping requirements.

The importance of additive manufacturing is not limited only to the ability to produce complex geometries. This technology also stands out with its advantages such as reducing material waste, eliminating the need for molds, responding rapidly to design modifications, and shortening product development processes. Especially in the early stages of product development, the ability to rapidly transform a design into a physical model provides an important advantage in terms of engineering validation and design revisions. In addition, the design freedom provided by additive manufacturing enables the production of hollow, lattice, topology-optimized, and functional geometries that are difficult, costly, or impossible to manufacture using conventional methods. Therefore, additive manufacturing has evolved from being an auxiliary technology used only for prototype production into a manufacturing approach that is directly used for functional part production in certain fields.

As shown in Figure 1, the application areas of additive manufacturing are quite broad. The production of lightweight and complex-geometry parts in the aerospace industry, rapid prototyping and customized component production in the automotive sector, and the fabrication of anatomical models, implants, tissue scaffolds, and patient-specific medical products in the biomedical field are among the important application areas of this technology (Chu et al., 2008; L. J. Kumar & Krishnadas Nair, 2016; Prashar et al., 2023). In addition, additive manufacturing is also used in fields such as architecture, defense, textiles, education, electronics, robotics, and mold making (Calignano et al., 2017; Gao et al., 2015; Prashar et al., 2023).

Figure 1. Application areas of additive manufacturing

Additive manufacturing methods are classified into different groups depending on the type of material used, the layer formation mechanism, and the energy source. In general, they are classified under material jetting, material extrusion, powder bed fusion, and directed energy deposition methods (Prashar et al., 2023; Vyavahare et al., 2020). Within this classification, the Fused Deposition Modeling (FDM) method, which belongs to the material extrusion group, is one of the most widely used techniques among additive manufacturing methods. The main reasons for this widespread use are the relatively low cost of the system, its applicability with desktop devices, its user-friendly production environment, and its compatibility with a wide range of thermoplastic filaments (Durgun & Ertan, 2014; Jaisingh Sheoran & Kumar, 2020; Pu'ad et al., 2020).

As shown in Figure 2, the FDM method is based on the principle of extruding a thermoplastic material in filament form through a heated nozzle in a semi-molten state and depositing it layer by layer. In this method, many polymer-based materials such as PLA (polylactic acid), ABS (acrylonitrile butadiene styrene), PETG (polyethylene terephthalate glycol), TPU (thermoplastic polyurethane), PA (polyamide), and various composite filaments can be used. Low initial investment cost, low material cost, a relatively safe working environment, easy material replacement, and rapid prototyping capability contribute to the widespread use of FDM technology in academic research, education, product development, and small-scale functional part production.

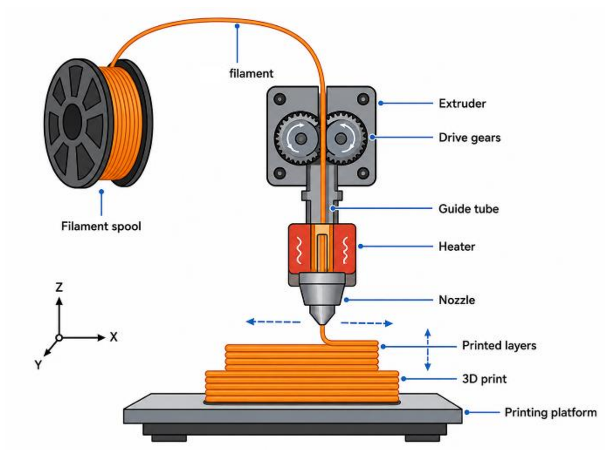

Figure 2. Schematic illustration of the FDM process

However, FDM technology also has certain limitations. Parts produced by this method generally exhibit anisotropic mechanical behavior due to their layered structure, and the quality of interlayer bonding directly affects the final strength (Liu et al., 2017; Rajan et al., 2022; Redwood et al., 2017). In addition, issues such as surface roughness, void formation, dimensional accuracy, warping, layer separation, and long production time are among the limitations that should be carefully considered in engineering applications of FDM parts (R. Kumar et al., 2021; Oztan et al., 2019). Therefore, the performance of parts produced by FDM technology does not depend only on the material used. Production parameters such as layer thickness, infill density, infill pattern, raster angle, build orientation, nozzle temperature, bed temperature, printing speed, and cooling conditions also significantly determine part quality and mechanical behavior (Dey & Yodo, 2019; Redwood et al., 2017).

As a result, FDM technology holds an important position within additive manufacturing in terms of the opportunities it offers for polymer-based part production and the process–performance relationship. In FDM, the layer-by-layer shaping of thermoplastic filament requires the properties of the material used and the production parameters to be evaluated together. Therefore, the basic working principles of the method, the selection criteria of polymer-based materials used in FDM, and the effects of production parameters on part performance should be addressed in an interconnected manner.

2. Fundamental Principles of FDM Technology

FDM technology is regarded as one of the most widely used additive manufacturing methods, applicable across a broad range of printers from low-cost devices to industrial systems. As shown in Figure 3, the FDM production process consists of consecutive digital preparation and manufacturing steps, starting from CAD modeling and continuing until the final printed part is obtained. In the first stage, the part geometry is created using CAD software, and this model is then generally converted into STL format. The STL file defines the part surface using numerous surface elements and enables the model to be processed by slicing software. During the slicing stage, the three-dimensional model is divided into specific layer thicknesses. At this stage, the build orientation, infill density, support structures, and nozzle movement paths are defined. The G-code file generated at the end of this process is used as the basic production data that determines the movement direction of the print head, printing speed, extrusion amount, and layer formation sequence. Subsequently, the filament is fed from the spool to the extruder, brought into a semi-molten state in the heated nozzle, and deposited layer by layer on the build platform to form the final part.

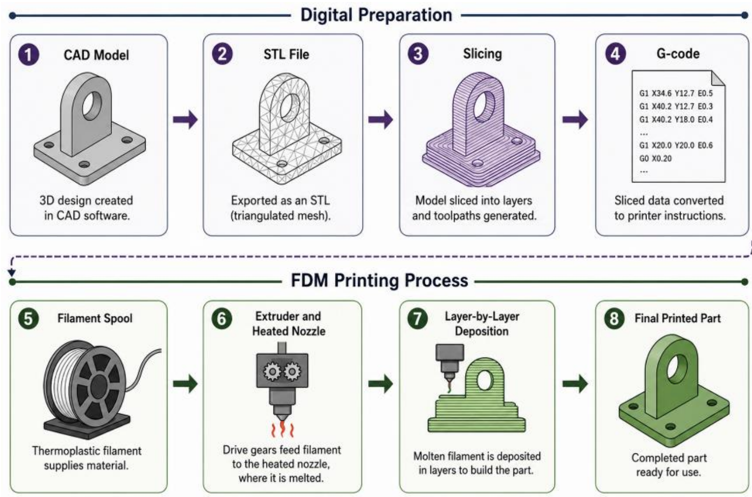

Figure 3. Schematic workflow of the FDM process from CAD modeling to final printed part

In FDM systems, the viscosity, flow behavior, and temperature sensitivity of the filament material become decisive for production stability. While very low viscosity may cause the material to lose its shape on the build platform, very high viscosity may make uniform extrusion difficult and lead to filament feeding problems. Therefore, in the FDM process, the viscosity-dependent flow behavior of the material is a fundamental factor that affects not only its exit from the nozzle but also interlayer bonding and the dimensional accuracy of the part (Pu'ad et al., 2020; W. Zhang et al., 2020). In this context, layer-by-layer production and part formation constitute the fundamental feature that makes FDM technology both advantageous and limited. Through this approach, complex geometries, hollow structures, and parts with different infill densities can be produced. However, the same layered structure also causes discontinuities and direction-dependent properties within the part. When each layer is deposited onto the previous layer while the material is still hot, better fusion can occur. If the material cools too rapidly or if the temperature of the previous layer is not sufficient, interlayer bonding may weaken (Jaisingh Sheoran & Kumar, 2020; Monzón et al., 2015). This situation may lead to layer separation, delamination, or brittle fracture behavior, especially under mechanical loading conditions such as tensile, flexural, and impact loading (Liu et al., 2017). Interlayer bonding mainly occurs through the contact of hot polymer roads, limited diffusion of molecular chains across the interface, solidification of the material upon cooling, and the formation of mechanical integrity between adjacent roads (Monzón et al., 2015; Pu'ad et al., 2020). The quality of bonding between layers is affected by nozzle temperature, bed temperature, ambient temperature, printing speed, cooling conditions, and material properties. Higher temperature can generally increase molecular mobility and interfacial fusion, but excessively high temperature may cause polymer degradation, flow instability, loss of detail, and deterioration of dimensional accuracy (Rajan et al., 2022; W. Zhang et al., 2020). Therefore, the FDM process should be carried out within a balanced processing window in which the material is sufficiently flowable but can still retain its shape after deposition.

The layered structure of FDM parts causes anisotropy in terms of mechanical behavior. The mechanical strength of a part produced with the same material and the same geometry may vary depending on whether the load is applied parallel or perpendicular to the layers (Rajan et al., 2022; Redwood et al., 2017). When loading is applied parallel to the layers, the load is mostly carried through the filament roads, whereas when loading is applied perpendicular to the layers, the strength of the interlayer interfaces becomes more decisive. Therefore, in the design of FDM parts, not only the part geometry but also the build orientation and loading direction should be evaluated together. Especially in functional parts, incorrect selection of build orientation and raster angle may result in a load-bearing capacity much lower than the nominal strength of the material (Ćwikła et al., 2017; Dudescu & Racz, 2017; Garzon-Hernandez et al., 2020). Considering the fundamental principles of FDM technology, it is seen that this method is not merely a simple layer deposition process. The production process is a holistic procedure consisting of digital preparation and printing stages. Each step may affect the surface quality, dimensional accuracy, internal void structure, and mechanical performance of the final part.

3. Polymer-Based Materials Used in FDM and Their Selection

The most commonly used materials in FDM technology are thermoplastic polymers. As shown in Figure 4, the most widely used among these include PLA, ABS, PETG, TPU, and PA, as well as various filled or reinforced filament materials. Since thermoplastics are materials that soften or melt when heated and solidify again when cooled, they are suitable for being fed in filament form and shaped by extrusion through a nozzle (Gibson et al., 2015; Mohan et al., 2017). The usability of these materials in the FDM process does not depend only on their melting or glass transition temperature. The viscosity, thermal stability, cooling behavior, moisture sensitivity, shrinkage tendency, interlayer bonding capability, and mechanical properties required for the target application should also be considered (Rajan et al., 2022; W. Zhang et al., 2020). Therefore, material selection for FDM should be evaluated as a balance between ease of production and final part performance.

Figure 4. Most commonly used filament materials

PLA is one of the most widely used polymers in FDM technology. Due to its easy printability, low warping tendency, bio-based origin, and relatively good stiffness, it is widely preferred, especially in desktop FDM printers. The fact that PLA can be processed at relatively low temperatures during printing and can adhere more easily to the build platform makes it an advantageous material for prototyping and low-load-bearing applications. However, PLA is not suitable for every engineering application because it generally exhibits more brittle behavior, low heat resistance, and limited impact strength (Mohan et al., 2017; D. Zhang et al., 2016).

ABS has certain advantages over PLA in terms of impact strength, toughness, heat resistance, and chemical resistance. Owing to these properties, ABS is widely used in the production of toys, household items, housings, prototypes, automotive parts, and engineering samples (Khan et al., 2021). However, ABS has a higher tendency to warp during printing than PLA and generally requires a heated bed or an enclosed printing chamber. In addition, since sufficient pressure is not applied during the FDM process, internal voids may form in ABS parts, and reducing these voids is important for better interlayer bonding and higher mechanical performance.

PETG has become increasingly common in FDM applications in recent years because it has a property profile that can be considered between PLA and ABS. PETG generally stands out with good chemical resistance, low shrinkage tendency, relatively high impact strength, and more stable printing behavior

(Khan et al., 2021). Studies on PETG have reported that infill density has a significant effect on tensile strength, that tensile strength may increase with increasing infill density, and that lower surface roughness can be obtained at high infill density (Dave et al., 2021; Dudescu & Racz, 2017). This indicates that the amount of internal voids and the contact area between filament roads are important for the final performance of materials such as PETG.

TPU is a thermoplastic polyurethane-based material with flexible and elastomeric properties. In FDM applications, TPU is preferred, especially for seals, flexible connectors, vibration-damping components, medical prototypes, and functional flexible parts due to its flexibility, wear resistance, impact damping capacity, and elastic deformation capability (Haryńska et al., 2018). However, printing flexible filaments such as TPU is more difficult than printing PLA or ABS. The flexibility of the filament may cause problems such as buckling inside the extruder, irregular feeding, and flow instability. Therefore, in TPU printing, the filament path, printing speed, nozzle temperature, and extruder type should be carefully selected.

PA or nylon group polymers hold an important place in FDM technology due to their high toughness, good impact strength, wear resistance, and mechanical properties suitable for engineering applications. Nylon materials are used especially for functional parts, gears, connectors, components exposed to friction, and composite filament matrices. However, PA materials have a high tendency to absorb moisture, and moist filament may cause problems such as vapor formation, surface defects, porosity, and reduction in mechanical properties during printing (Aslanzadeh et al., 2018; Calignano et al., 2020). Therefore, it is important to dry PA filaments before printing and store them under suitable conditions.

In FDM technology, not only neat polymers but also reinforced and composite filaments are increasingly used. Reinforcements such as carbon fiber, glass fiber, graphene, carbon nanotubes, metal powders, ceramic particles, wood flour, and natural fibers are added to polymer matrices in order to obtain higher stiffness, strength, electrical conductivity, thermal stability, or functional properties (Acierno & Patti, 2023). Although composite filaments have the potential to improve the limited mechanical properties of neat polymers, printing these materials is a more complex process. Fiber or particle reinforcements may cause nozzle wear, flow irregularities, filament breakage, non-uniform fiber distribution, and weak bonding between the matrix and the reinforcement. Therefore, in composite filaments, not only the type and amount of reinforcement but also filament production quality, fiber orientation, nozzle temperature, printing speed, and layer bonding become decisive for performance.

The factors affecting material selection should be evaluated according to the intended use of the part to be produced. While easy printability and low cost come to the forefront in visual prototypes or educational parts, properties such as tensile strength, elastic modulus, impact strength, fatigue behavior, heat resistance, and dimensional stability become more important in functional parts. Although PLA is advantageous in terms of easy printing and stiffness, it may remain limited in applications requiring high temperature resistance or impact performance. ABS is a strong option in terms of toughness and heat resistance, but it is more sensitive in terms of warping and printing environment control. PETG offers a balanced option in terms of chemical resistance and low shrinkage, while TPU can be preferred for flexible applications and PA for parts requiring high toughness and wear resistance (Khan et al., 2021). Material selection is also evaluated in terms of sustainability. The conversion of thermoplastics such as recycled PLA, ABS, PET, PP, and HDPE into filaments for FDM is an important research area for the reuse of plastic waste (Chapiro, 2016; Kai, 1994). Therefore, the use of recycled filaments is promising in terms of sustainability, but it requires material characterization and process optimization.

In general, polymer material selection in FDM technology requires the combined consideration of printability, cost, mechanical performance, thermal behavior, surface quality, dimensional stability, environmental resistance, and sustainability parameters. Therefore, material and process should not be considered independently in FDM technology. The properties of the material directly determine the production process, and the production process directly determines the performance of the final part.

4. FDM Production Parameters and Their Effects on Part Performance

In FDM technology, production parameters are among the fundamental variables that determine the mechanical and functional performance of the final part. Even when the same material, the same geometry, and the same printer are used, changes in layer thickness, infill density, infill pattern, raster angle, build orientation, nozzle temperature, bed temperature, printing speed, and cooling conditions may create different void ratios, different interlayer bonding, different surface quality, and different mechanical behavior within the part. Therefore, in the evaluation of FDM parts, it is not sufficient to specify only the material type. Production parameters should also be clearly defined, and performance interpretations should be associated with these parameters.

Layer thickness is one of the most fundamental parameters in FDM production. As shown in Figure 5, layer thickness determines the height of the layer formed during each pass of the nozzle and directly affects both production time and surface quality. Lower layer thickness generally provides better surface quality, a reduced stair-stepping effect, and higher geometrical resolution. However, since the number of layers increases, the production time also increases significantly (Barrios & Romero, 2019; Ian Gibson, 2015). Higher layer thickness, on the other hand, may reduce production time, but it may increase surface roughness, change the contact area between layers, and affect internal void formation (Barrios & Romero, 2019; Vu et al., 2018). In the literature, it has been reported that an increase in layer height may, in some cases, lead to greater void formation and reduce tensile strength (Garzon-Hernandez et al., 2020; Vu et al., 2018).

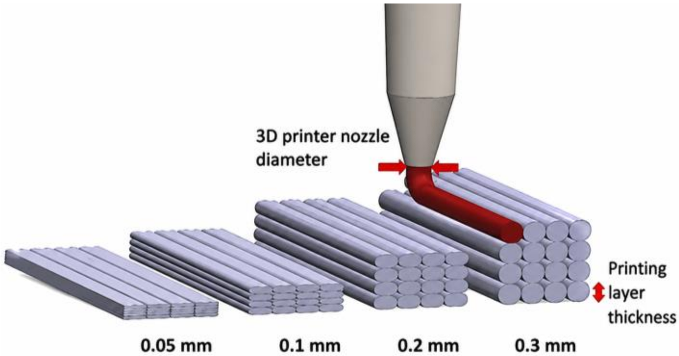

Figure 5. Schematic illustration of layer thickness (Ayrilmis, 2018)

Infill density (Figure 6) is an important parameter that determines how much of the internal volume of the part will be filled with material. While low infill density reduces material consumption, production time, and part weight, high infill density generally increases stiffness, strength, and energy absorption capacity (Dave et al., 2021; Dudescu & Racz, 2017). Studies on polymer parts such as PETG and PLA have reported that tensile strength may increase as infill density increases, higher mechanical performance can be obtained at full infill, and the amount of internal voids has a significant effect on mechanical behavior (Dave et al., 2021; Liu et al., 2017). This result shows how decisive the air gaps between filament roads and the internal structure are in terms of mechanical performance. However, high infill density may not always be the best option for all performance criteria. Higher infill density may increase production time and material cost, and in some cases, it may also affect residual stress accumulation or dimensional deviation (Dudescu & Racz, 2017). Therefore, when selecting infill density, part weight, strength, production time, and intended use should be evaluated together.

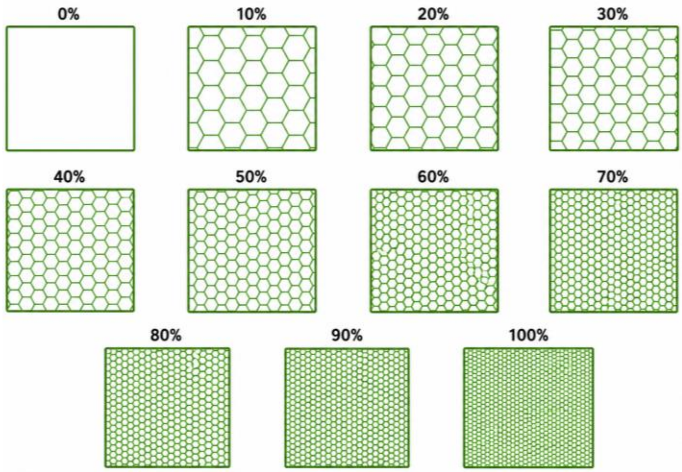

Figure 6. Example illustration of different infill densities

Infill pattern (Figure 7) is another important parameter that determines the geometrical arrangement of the internal structure and affects load transfer paths. Different infill patterns such as grid, rectilinear, honeycomb, triangular, gyroid, and concentric may affect the stiffness, strength, deformation, and energy absorption behavior of the part in different ways (Dave et al., 2021; Dudescu & Racz, 2017). The infill pattern determines not only the arrangement of internal voids but also the directions through which the load is carried within the part. In the literature, some studies have reported that hexagonal or triangular infill patterns may provide advantages in terms of certain mechanical properties, but maximum mechanical strength with minimum dimensional error may not always be obtained with the same parameter combination. This indicates that optimization in FDM production should be multi-objective rather than single-objective. While a parameter combination may give good results in terms of tensile strength, the same combination may not be the most suitable option in terms of surface quality or dimensional accuracy (Dudescu & Racz, 2017).

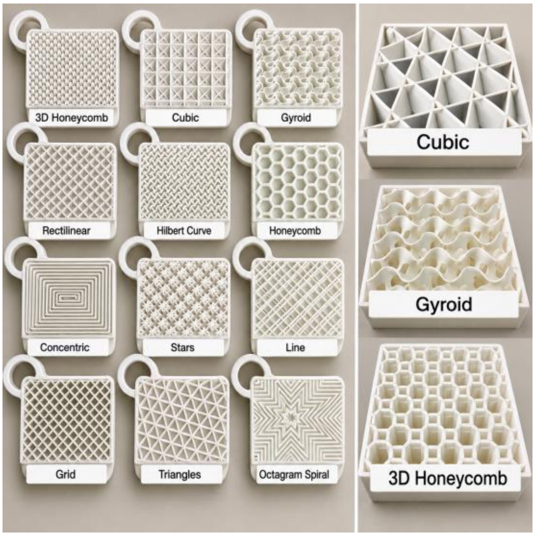

Figure 7. Examples of infill patterns used in FDM printing (Lopes et al., 2023)

Raster angle (Figure 8) has a direct effect on mechanical performance because it determines the orientation of filament roads with respect to the loading direction. When the raster angle is 0°, the filament roads are generally positioned parallel to the loading direction, and the load is mostly carried by continuous filaments. When the raster angle is 90°, load transfer becomes more dependent on the bonds between filaments and the interlayer interfaces (Durgun & Ertan, 2014; Garzon-Hernandez et al., 2020). Therefore, delamination and layer separation may become more dominant damage mechanisms in parts with a 90° raster orientation (Liu et al., 2017). This result indicates that, in the mechanical design of FDM parts, the raster angle should be selected together with the loading direction.

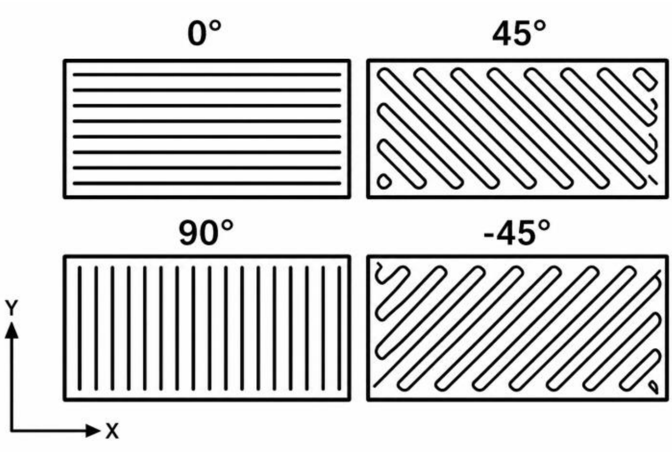

Figure 8. Example illustration of different raster angles

Build orientation or production orientation (Figure 9) determines the position in which the part will be produced on the build platform. Different build orientations such as flat, on-edge, and upright affect mechanical performance because they change the position of the layers with respect to the loading direction. When the part is produced in a way that carries the load parallel to the layers, higher strength may be obtained, whereas strength may decrease in orientations where the interlayer bonding is directly stressed (Raut et al., 2014; Ziemian et al., 2015). Build orientation also affects surface roughness, support material requirement, production time, and dimensional accuracy. Therefore, when selecting the build orientation, not only mechanical strength but also the amount of support, the quality of critical surfaces, and the service conditions of the part should be considered (Al-Ahmari et al., 2018; Dani et al., 2013).

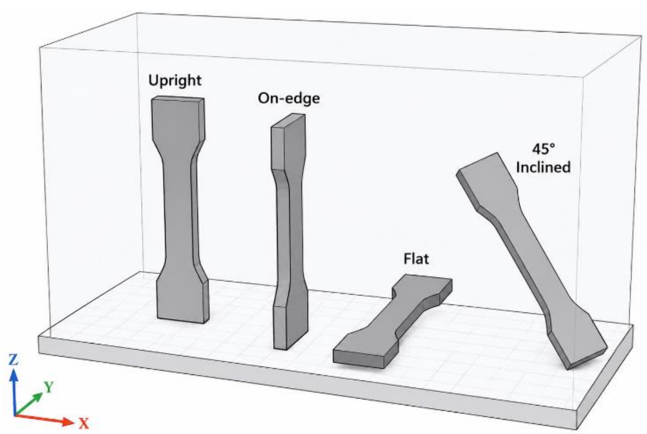

Figure 9. Example build and production orientations

Nozzle temperature is another parameter that affects the flowability of the material, interlayer fusion, and surface quality. When the nozzle temperature is too low, the material cannot become fully flowable, extrusion may become unstable, and interlayer bonding may remain weak. When the nozzle temperature is within an appropriate range, the material spreads better, makes better contact with the previous layer, and stronger interfacial bonds may form. However, excessively high temperature may cause polymer degradation, excessive flow, loss of detail, and reduced geometrical accuracy (Pu'ad et al., 2020; Rajan et al., 2022; W. Zhang et al., 2020). Although some studies have reported that higher nozzle temperature may have positive effects on stiffness, strength, and ductility, it should be noted that this effect depends on the material type and other parameters.

Bed temperature is particularly effective on first-layer adhesion, warping behavior, and dimensional stability. In materials with a high shrinkage tendency, such as ABS, insufficient bed temperature may cause corner lifting, separation in the lower layers, and overall warping (Singh, 2018). Since bed temperature affects the cooling rate of the material, it also contributes to controlling temperature differences between layers. However, when the bed temperature is selected too high, excessive softening in the lower layers, geometrical deformation, or surface deterioration may occur. Therefore, bed temperature should be determined by considering the glass transition temperature of the material, the printing environment, and the part geometry.

Printing speed creates a direct balance between production time and part quality. High printing speed reduces production time, but it may make it difficult for the material to exit the nozzle regularly, to be deposited on the layer with sufficient contact, and to fuse with the previous layer. Low printing speed may provide better layer deposition and surface quality, but it increases production time and may cause excessive heat accumulation in some materials. In the literature, it is stated that the correct combination between printing speed, temperature, and viscosity is decisive for ensuring continuous and stable material flow from the nozzle (Bakarich et al., 2014; Peng et al., 2021; W. Zhang et al., 2020).

Cooling rate and fan use may produce different results in FDM production, especially for materials such as PLA and ABS. While controlled fan use in PLA printing may improve surface quality and detail accuracy, rapid cooling in ABS printing may increase the risk of warping and layer separation. Since cooling conditions determine the solidification time of the layers, interfacial diffusion, and residual stress formation, they are directly related to mechanical performance. Very rapid cooling may cause solidification before sufficient fusion occurs between layers. Very slow cooling may impair geometrical stability or reduce detail accuracy. Therefore, fan ratio and ambient temperature should be adjusted according to the thermal behavior of the material used.

The relationship between production parameters and mechanical and functional performance is one of the most fundamental research areas of FDM technology. In the literature, build orientation, layer height, infill density, and raster angle are reported to be important parameters for improving static mechanical properties (Garzon-Hernandez et al., 2020; Redwood et al., 2017). In addition, extrusion temperature, number of walls, and printing speed are among the other variables that affect performance (Dey & Yodo, 2019; Peng et al., 2021). The effects of these parameters are often not independent of each other. Defect formation in FDM-printed parts is also closely related to parameter selection. Shape distortion, residual stresses, micro voids, non-uniform fiber distribution in fiber-reinforced filaments, weak bonding between the matrix and fibers, and surface roughness associated with the stair-stepping effect are among the most common defects. These defects may affect not only the appearance but also tensile strength, fracture toughness, impact behavior, and fatigue performance (Barrios & Romero, 2019; Oztan et al., 2019). Therefore, producing a good part using FDM technology does not simply mean obtaining the part from the printer. The voids formed inside the part, interlayer bonding, surface quality, and load transfer paths should be analyzed together with the production parameters.

In general, layer thickness, infill density, infill pattern, and raster angle can be considered the most prominent parameters determining the performance of FDM parts. However, build orientation, nozzle temperature, bed temperature, printing speed, and cooling conditions are also complementary variables that may strengthen or weaken the effects of these parameters. Therefore, for reliable part production with FDM, parameters should not be regarded only as default printer settings, but should be consciously selected according to the targeted mechanical and functional performance. In functional applications, production parameters should be experimentally verified and, where possible, supported by mechanical test results. In this way, FDM technology can be used not only as a rapid prototyping tool but also as an engineering method that enables controlled and repeatable part production.

5. Conclusions

FDM technology stands out as a low-cost, accessible, and flexible additive manufacturing method for the production of polymer-based parts. Its ability to produce physical parts directly from a digital model, its compatibility with different thermoplastic filaments, and its ability to facilitate the production of complex geometries have been decisive in the widespread use of this method. However, the performance of parts produced by FDM does not depend only on the material used. The layered production structure, build orientation, interlayer bonding, and selected process parameters directly affect the final part behavior.

The evaluations presented in this chapter show that FDM technology should not be regarded as a simple plastic extrusion process. The production process is an engineering approach in which the relationship between material selection, printer settings, layer formation, internal structure arrangement, and part performance is managed together. Therefore, the selected production parameters should be considered as fundamental variables that determine the mechanical and functional properties of the part.

In FDM technology, different polymer-based materials such as PLA, ABS, PETG, TPU, PA, and reinforced filaments offer different advantages depending on the intended use. However, each material has different printing behavior, interlayer bonding capability, warping tendency, and mechanical performance. Therefore, for reliable part production, material selection and production parameters should be evaluated together. Especially in functional part production, selecting production parameters without considering the loading conditions and service environment to which the part will be exposed may prevent the expected performance from being achieved.

In general, FDM technology offers strong potential for the production of polymer-based parts with the correct material and suitable process parameters. However, limitations such as interlayer bonding, void formation, surface quality, dimensional accuracy, and anisotropic behavior should be taken into account. Therefore, for FDM-produced parts to be used more reliably in engineering applications, production parameters should be selected consciously, experimentally verified when necessary, and part performance should be evaluated from a holistic perspective.

References

Acierno, D. & Patti, A. (2023). Fused Deposition Modelling (FDM) of Thermoplastic-Based Filaments: Process and Rheological Properties—An Overview. In *Materials* (Vol. 16, Issue 24). Multidisciplinary Digital Publishing Institute (MDPI). https://doi.org/10.3390/ma16247664

Al-Ahmari, A. M., Abdulhameed, O. & Khan, A. A. (2018). An automatic and optimal selection of parts orientation in additive manufacturing. *Rapid Prototyping Journal*, *24*(4), 698–708.

Aslanzadeh, S., Saghlatoon, H., Honari, M. M., Mirzavand, R., Montemagno, C. & Mousavi, P. (2018). Investigation on electrical and mechanical properties of 3D printed nylon 6 for RF/microwave electronics applications. *Additive Manufacturing*, *21*, 69–75.

Ayrilmis, N. (2018). Effect of layer thickness on surface properties of 3D printed materials produced from wood flour/PLA filament. *Polymer Testing*, *71*, 163–166. https://doi.org/10.1016/j.polymertesting.2018.09.009

Bakarich, S. E., Gorkin III, R., in het Panhuis, M. & Spinks, G. M. (2014). Three-dimensional printing fiber reinforced hydrogel composites. *ACS Applied Materials & Interfaces*, *6*(18), 15998–16006.

Barrios, J. M. & Romero, P. E. (2019). Improvement of surface roughness and hydrophobicity in PETG parts manufactured via fused deposition modeling (FDM): an application in 3D printed self–cleaning parts. *Materials*, *12*(15), 2499.

Calignano, F., Lorusso, M., Roppolo, I. & Minetola, P. (2020). Investigation of the mechanical properties of a carbon fibre-reinforced nylon filament for 3D printing. *Machines*, *8*(3), 52.

Calignano, F., Manfredi, D., Ambrosio, E. P., Biamino, S., Lombardi, M., Atzeni, E., Salmi, A., Minetola, P., Iuliano, L. & Fino, P. (2017). Overview on additive manufacturing technologies. *Proceedings of the IEEE*, *105*(4), 593–612.

Chapiro, M. (2016). Current achievements and future outlook for composites in 3D printing. *Reinforced Plastics*, *60*(6), 372–375.

Chu, C., Graf, G. & Rosen, D. W. (2008). Design for additive manufacturing of cellular structures. *Computer-Aided Design and Applications*, *5*(5), 686–696.

Ćwikła, G., Grabowik, C., Kalinowski, K., Paprocka, I. & Ociepka, P. (2017). The influence of printing parameters on selected mechanical properties of FDM/FFF 3D-printed parts. *IOP Conference Series: Materials Science and Engineering*, *227*(1). https://doi.org/10.1088/1757-899X/227/1/012033

Dani, T., Kamdi, P., Nalamwar, G. & Borse, V. (2013). Multi objective optimization of built orientation for rapid prototyping of connecting rod. *International Journal of Scientific Research and Management*, *1*(1), 13–18.

Dave, H. K., Patadiya, N. H., Prajapati, A. R. & Rajpurohit, S. R. (2021). Effect of infill pattern and infill density at varying part orientation on tensile properties of fused deposition modeling-printed poly-lactic acid part. *Proceedings of the Institution of Mechanical Engineers, Part C: Journal of Mechanical Engineering Science*, *235*(10), 1811–1827.

De Leon, A. C., Chen, Q., Palaganas, N. B., Palaganas, J. O., Manapat, J. & Advincula, R. C. (2016). High performance polymer nanocomposites for additive manufacturing applications. *Reactive and Functional Polymers*, *103*, 141–155.

Dey, A. & Yodo, N. (2019). A systematic survey of FDM process parameter optimization and their influence on part characteristics. *Journal of Manufacturing and Materials Processing*, *3*(3), 64.

Dudescu, C. & Racz, L. (2017). Effects of Raster Orientation, Infill Rate and Infill Pattern on the Mechanical Properties of 3D Printed Materials. *ACTA Universitatis Cibiniensis*, *69*(1), 23–30. https://doi.org/10.1515/aucts-2017-0004

Durgun, I. & Ertan, R. (2014). Experimental investigation of FDM process for improvement of mechanical properties and production cost. *Rapid Prototyping Journal*, *20*(3), 228–235.

Gao, W., Zhang, Y., Ramanujan, D., Ramani, K., Chen, Y., Williams, C. B., Wang, C. C. L., Shin, Y. C., Zhang, S. & Zavattieri, P. D. (2015). The status, challenges, and future of additive manufacturing in engineering. *Computer-Aided Design*, *69*, 65–89. https://doi.org/https://doi.org/10.1016/j.cad.2015.04.001

Garzon-Hernandez, S., Garcia-Gonzalez, D., Jérusalem, A. & Arias, A. (2020). Design of FDM 3D printed polymers: An experimental-modelling methodology for the prediction of mechanical properties. *Materials & Design*, *188*, 108414.

Gibson, I., Rosen, D. & Stucker, B. (2015). *Additive manufacturing technologies: 3D printing, rapid prototyping, and direct digital manufacturing*. Springer.

Haryńska, A., Gubanska, I., Kucinska-Lipka, J. & Janik, H. (2018). Fabrication and characterization of flexible medical-grade TPU filament for Fused Deposition Modeling 3DP technology. *Polymers*, *10*(12). https://doi.org/10.3390/polym10121304

Ian Gibson, I. G. (2015). *Additive manufacturing technologies 3D printing, rapid prototyping, and direct digital manufacturing*. Springer.

Jaisingh Sheoran, A. & Kumar, H. (2020). Fused Deposition modeling process parameters optimization and effect on mechanical properties and part quality: Review and reflection on present research. *Materials Today: Proceedings*, *21*, 1659–1672. https://doi.org/https://doi.org/10.1016/j.matpr.2019.11.296

Kai, C. C. (1994). Three-dimensional rapid prototyping technologies and key development areas. *Computing and Control Engineering*, *5*(4), 200–206.

Khan, S., Joshi, K. & Deshmukh, S. (2021). A comprehensive review on effect of printing parameters on mechanical properties of FDM printed parts. *Materials Today: Proceedings*, *50*, 2119–2127. https://doi.org/10.1016/j.matpr.2021.09.433

Kumar, L. J. & Krishnadas Nair, C. G. (2016). Current trends of additive manufacturing in the aerospace industry. In *Advances in 3D printing & additive manufacturing technologies* (pp. 39–54). Springer.

Kumar, R., Kumar, M. & Chohan, J. S. (2021). Material-specific properties and applications of additive manufacturing techniques: a comprehensive review. *Bulletin of Materials Science*, *44*(3), 181.

Liu, R., Wang, Z., Sparks, T., Liou, F. & Newkirk, J. (2017). Aerospace applications of laser additive manufacturing. In *Laser additive manufacturing* (pp. 351–371). Elsevier.

Lopes, L., Reis, D., Paula Junior, A. & Almeida, M. (2023). Influence of 3D Microstructure Pattern and Infill Density on the Mechanical and Thermal Properties of PET-G Filaments. *Polymers*, *15*(10). https://doi.org/10.3390/polym15102268

Mohan, N., Senthil, P., Vinodh, S. & Jayanth, N. (2017). A review on composite materials and process parameters optimisation for the fused deposition modelling process. *Virtual and Physical Prototyping*, *12*(1), 47–59.

Monzón, M. D., Ortega, Z., Martínez, A. & Ortega, F. (2015). Standardization in additive manufacturing: activities carried out by international organizations and projects. *The International Journal of Advanced Manufacturing Technology*, *76*(5), 1111–1121.

Oztan, C., Karkkainen, R., Fittipaldi, M., Nygren, G., Roberson, L., Lane, M. & Celik, E. (2019). Microstructure and mechanical properties of three dimensional-printed continuous fiber composites. *Journal of Composite Materials*, *53*(2), 271–280.

Patti, A., Acierno, S., Cicala, G., Zarrelli, M. & Acierno, D. (2022). Recovery of waste material from biobags: 3D printing process and thermo-mechanical characteristics in comparison to virgin and composite matrices. *Polymers*, *14*(10), 1943.

Peng, W., Bin, Z. O. U., Shouling, D. & Lei, L. I. (2021). Effects of FDM-3D printing parameters on mechanical properties and microstructure of CF/PEEK and GF/PEEK. *Chinese Journal of Aeronautics*, *34*(9), 236–246.

Prashar, G., Vasudev, H. & Bhuddhi, D. (2023). Additive manufacturing: expanding 3D printing horizon in industry 4.0. *International Journal on Interactive Design and Manufacturing (IJIDeM)*, *17*(5), 2221–2235.

Pu'ad, N. A. S. M., Haq, R. H. A., Noh, H. M., Abdullah, H. Z., Idris, M. I. & Lee, T. C. (2020). Review on the fabrication of fused deposition modelling (FDM) composite filament for biomedical applications. *Materials Today: Proceedings*, *29*, 228–232.

Rajan, K., Samykano, M., Kadirgama, K., Harun, W. S. W. & Rahman, M. M. (2022). Fused deposition modeling: process, materials, parameters, properties, and applications. *The International Journal of Advanced Manufacturing Technology*, *120*(3), 1531–1570.

Raut, S., Jatti, V. S., Khedkar, N. K. & Singh, T. P. (2014). Investigation of the effect of built orientation on mechanical properties and total cost of FDM parts. *Procedia Materials Science*, *6*, 1625–1630.

Redwood, B., Schffer, F. & Garret, B. (2017). *The 3D printing handbook: technologies, design and applications*. 3D Hubs.

Singh, K. (2018). Experimental study to prevent the warping of 3D models in fused deposition modeling. *International Journal of Plastics Technology*, *22*(1), 177–184.

Vu, I. Q., Bass, L. B., Williams, C. B. & Dillard, D. A. (2018). Characterizing the effect of print orientation on interface integrity of multi-material jetting additive manufacturing. *Additive Manufacturing*, *22*, 447–461.

Vyavahare, S., Teraiya, S., Panghal, D. & Kumar, S. (2020). Fused deposition modelling: a review. In *Rapid Prototyping Journal* (Vol. 26, Issue 1, pp. 176–201). Emerald Group Holdings Ltd. https://doi.org/10.1108/RPJ-04-2019-0106

Zhang, D., Chi, B., Li, B., Gao, Z., Du, Y., Guo, J. & Wei, J. (2016). Fabrication of highly conductive graphene flexible circuits by 3D printing. *Synthetic Metals*, *217*, 79–86.

Zhang, W., Chen, J. & Zeng, H. (2020). Polymer processing and rheology. In *Polymer science and nanotechnology* (pp. 149–178). Elsevier.

Ziemian, S., Okwara, M. & Ziemian, C. W. (2015). Tensile and fatigue behavior of layered acrylonitrile butadiene styrene. *Rapid Prototyping Journal*, *21*(3), 270–278.

Chapter 5

Sustainable Aquaponic Systems: A Review of Design, Resource Efficiency, and Nutrient Recovery

Şevval ŞENDAL[1], Güray ÇELİK[2], Nezih Kamil SALİHOĞLU[3]

ABSTRACT

Aquaponic systems are among the innovative production technologies that enable the simultaneous cultivation of fish and plants and facilitate the reuse of resources. By allowing plants to utilize nutrients such as nitrogen and phosphorus generated in aquaculture units, water consumption is reduced, the need for chemical fertilizers is significantly lowered, and the circular economy approach is supported through the reuse of waste. In this book chapter, the engineering design of aquaponic systems, investment and operating costs, energy and water use efficiency, as well as current approaches to fish sludge management and nutrient recovery are examined within the framework of a comprehensive literature review. Studies in the literature show that aquaponic systems offer significant advantages, particularly in terms of water use efficiency; however, high initial investment, energy requirements, and nutrient losses due to sludge are major limiting factors for the sustainability of these systems. In addition, innovative applications developed for the recovery of fish sludge were evaluated, and it was demonstrated that these technologies could make significant contributions to the development of closed-loop production systems by improving resource efficiency. In conclusion, it is believed that, in order to enhance the potential of aquaponic systems for sustainable food production and circular economy applications, it is necessary to develop integrated system designs that are highly energy-efficient, have low water consumption, and feature optimized nutrient recovery.

Keywords: Aquaponic systems, recirculating aquaculture system (RAS), water efficiency, energy consumption, nutrient recovery, circular economy

---

[1] MSc Student, Bursa Uludağ University, Faculty of Engineering, Department of Environmental Engineering, Bursa, Turkey. ORCID: 0009-0006-5277-8377

[2] Prof. Dr., Bursa Uludağ University, Faculty of Engineering, Department of Environmental Engineering, Bursa, Turkey. ORCID: 0000-0003-0714-048X

[3] Prof. Dr., Bursa Uludağ University, Faculty of Engineering, Department of Environmental Engineering, Bursa, Turkey. ORCID: 0000-0002-7730-776X

1. Introduction

The world's population is growing rapidly every day, and it is projected to reach approximately 10 billion by 2050 (UN DESA, 2022). This situation is leading to an increase in food demand and putting pressure on natural resources (Godfray et al., 2010). For this reason, approaches that increase resource efficiency and reduce environmental impacts are becoming increasingly important for the future of food production systems.

Aquaponic systems are a production model that integrates hydroponic plant cultivation with fish farming systems known as recirculating aquaculture systems (Joyce et al., 2019; Lennard & Goddek, 2019). In these systems, the waste generated from fish farming is converted into nutrients that plants can utilize through the action of nitrifying bacteria; the plants, in turn, use these nutrients to filter the water, and the filtered water is then recirculated back to the fish-rearing unit (Joyce et al., 2019; Kim et al., 2005). In this way, a closed-loop production system is established in which water circulates continuously, thereby reducing water consumption and enabling production without the need for synthetic chemical fertilizers (Love et al., 2015).

One of the most significant advantages of aquaponic systems is the ability to simultaneously cultivate fish and crops within the same production system and to convert waste into a valuable resource during this process (Hu et al., 2015; Goddek et al., 2015). However, the sustainability of aquaponic systems is influenced by numerous engineering and operational parameters, such as design criteria, energy consumption, water management, operating costs, sludge management, and nutrient recovery efficiency (Zappernick et al., 2022; Guan et al., 2025; Love et al., 2015; Delaide et al., 2017; Madady et al., 2025).

In this book chapter, the current state of aquaponic systems is examined from a sustainability perspective, and recent developments in system design, investment and operating costs, energy and water use efficiency, fish sludge management, nutrient recovery, and circular economy applications are presented through a comprehensive review of the literature. Thus, the aim is to present an up-to-date perspective on the role of aquaponic systems in sustainable food production, as well as on future research directions and application areas.

2. Engineering Design of Sustainable Aquaponic Systems

2.1. Aquaponic System Configuration

Aquaponic systems are an innovative food production technology in which fish farming and plant cultivation are carried out together (Lennard & Goddek, 2019). In these systems, it is of great importance for the efficient and sustainable operation of the system that key components, such as fish tanks, mechanical and biological filtration units, water circulation lines, and hydroponic production modules, are designed to work together in an integrated and compatible manner (Espinal & Matulić, 2019; Lennard & Goddek, 2019). At the same time, it is necessary to continuously monitor and control water quality parameters, such as dissolved oxygen, ammonia, organic matter, CO_2, and nutrient balance, that determine system performance (Espinal & Matulić, 2019). An example of a small-scale aquaponic system designed by Love et al. (2015) is shown in Figure 1.

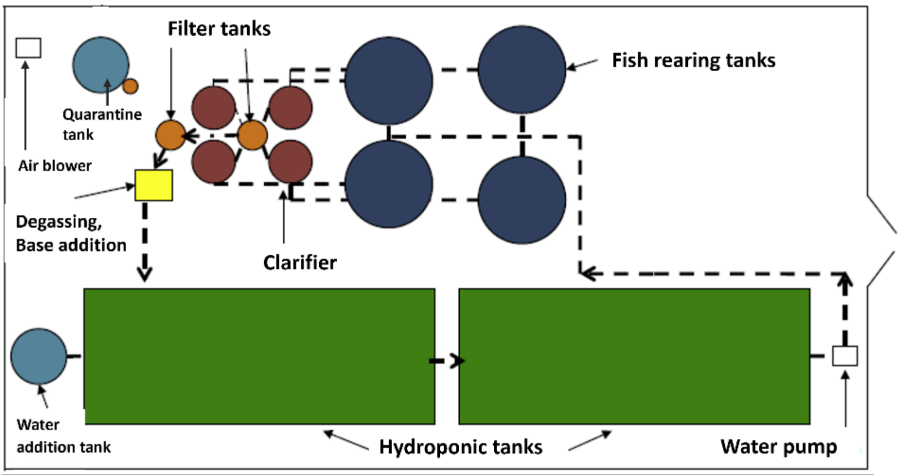

Tank Dimensions

Rearing tanks (×4): Water volume: 760 L each; dimensions: 0.84 m (height) × 1.22 m (diameter).
Clarifiers (×4): Water volume: 190 L each; dimensions: 1.12 m × 0.61 m.
Filter tanks (×2): Water volume: 132 L each; dimensions: 0.71 m (diameter) × 0.48 m.
Hydroponic tanks (×2): Dimensions: 5.5 m × 2.4 m × 0.22 m; total growing area: 13.4 m^2
Base addition tank (×1): Water volume: 190 L; dimensions: 0.30 m × 0.46 m × 0.64 m.
Water addition tank (×1): Water volume: 625 L.
Total system water volume: 10,280 L.
Flow rate: 93 L/min.
Total land area: 116 m^2.
Water pump head height: 1.2 m.

Figure 1. Flow diagram of a small-scale aquaponic system (Love et al., 2015)

A review of Figure 1 reveals that the system consists of fish-rearing tanks, filter tanks, a sedimentation unit, hydroponic production tanks, a water-supply unit, and a water pump. In aquaponic systems, the fish tanks provide the environment where the fish are raised, while the hydroponic tanks provide the environment where the plants are grown (Somerville, 2014). Solid matter that accumulates in the fish tank is removed using mechanical filtration units, and the nitrification processes necessary for nutrient recovery take place in biofilters (Somerville, 2014). In addition, pumps are used to circulate water between the units in the system, and aeration units are used to maintain the required concentration of dissolved oxygen in the system (Somerville, 2014).

In the literature, while high water and nutrient recovery rates and production efficiency stand out as significant advantages of aquaponic systems, high initial costs and energy requirements are among the major limiting factors (Lennard & Goddek, 2019; Asciuto et al., 2019; Babatunde et al., 2021; Guan et al., 2025; Love et al., 2015). For this reason, resource use efficiency in aquaponic systems and the extent to which the system's investment costs are economically offset by its production performance are of great importance.

2.2. Investment Cost

Aquaponic systems are considered production models that require a higher initial investment compared to traditional plant and fish production systems, due to the integration of fish farming and plant production components within the same system and the resulting need to install filtration, water circulation, and control equipment together (Zappernick et al., 2022; Asciuto et al., 2019; Babatunde et al., 2021; Ibrahim et al., 2023). In a study conducted on a medium-scale aquaponic system, a fish tank with a volume of 5,300 L and a plant cultivation tank with an average area of 63 m^2 were selected; it was noted that the initial investment cost was approximately \$69,230–\$69,600, and that the greenhouse structure accounted for approximately 42% of this cost (Zappernick et al., 2022). In this regard, it is evident that the investment cost of greenhouse infrastructure is one of the key components in medium-scale aquaponic systems.

The investment costs of aquaponic systems are not limited to equipment and infrastructure alone; they also include processes such as planning and installation. For example, in an analysis of a pilot-scale aquaponic system established under Mediterranean climate conditions, it was noted that the main components of the investment cost were planning, construction, and system installation (Asciuto et al., 2019). The study calculated the total initial investment cost at 1,647.60 euros; it was reported that approximately 475 euros of this amount consisted of expenses related to installation, design, and implementation (Asciuto et al., 2019). These findings indicate that, in addition to physical equipment, engineering design and installation processes also account for a significant portion of the initial investment costs in aquaponic systems.

When comparing the investment costs of different types of aquaponic systems, a correlation is observed between the production technology used and the cost. For example, in a study comparing deep water culture (DWC) systems with expanded clay aggregate (LECA)-based systems, it was noted that LECA-based systems have higher initial investment costs than DWC systems but offer better economic performance under appropriate production combinations (Petrea et al., 2016). This finding indicates that the choice of substrate and technology in aquaponic system design affects investment costs.

In aquaponic systems, the initial cost stands out as a significant economic factor not only for large-scale systems but also for low-cost aquaponic systems (Babatunde et al., 2021). In a study conducted in South Africa on low-cost aquaponic systems, determining the total capital cost was considered one of the key steps in profitability analyses (Babatunde et al., 2021). In addition, Somerville et al. (2014) note that, in order to ensure economic sustainability in aquaponic systems, the system's expected production performance must be evaluated in conjunction with its investment costs.

However, it has been noted that the adoption and widespread implementation of aquaponic systems by society are constrained due to the high initial costs of this technology (Ibrahim et al., 2023). In a comprehensive review, it was stated that high investment costs and technical complexity are the primary factors limiting the feasibility of large-scale, automation-based aquaponic systems (Ibrahim et al., 2023).

When the studies in the literature are evaluated collectively, it is observed that initial investment costs in aquaponic systems vary depending on system scale, the technology used, and infrastructure requirements, but are generally high (Zappernick et al., 2022; Asciuto et al., 2019; Babatunde et al., 2021; Petrea et al., 2016; Ibrahim et al., 2023). While greenhouse structures, treatment, and automation equipment account for a large portion of investment costs, system design and installation processes also play a significant role in the total cost (Asciuto et al., 2019; Zappernick et al., 2022). For this reason, the initial investment cost in aquaponic systems must be planned in a way that supports the system's economic return. Particularly when it comes to investments in equipment and infrastructure, it is important to choose alternatives that will increase the system's economic profitability.

2.3. Operation Cost

Operating costs in aquaponic systems are one of the most critical parameters determining the system's economic sustainability and vary depending on the labor, feed, energy, and other inputs used in the production process (Zappernick et al., 2022; Asciuto et al., 2019). In this context, various studies in the literature highlight the importance of labor requirements in aquaponic systems and their impact on operating costs (Zappernick et al., 2022; Asciuto et al., 2019). For example, it has been determined that the annual operating cost for a medium-scale aquaponic system is approximately $33,100–$33,300, and that 52% of this cost consists of labor expenses (Zappernick et al., 2022). This situation demonstrates that aquaponic systems are labor-intensive due to their nature, which requires a high level of monitoring and maintenance. In the economic analysis of a pilot-scale aquaponics system established under Mediterranean climatic conditions, it was determined that the operating expenses consisted of items such as maintenance, labor, energy, water, fish feed, fingerlings, and seedling procurement; the total operating cost was calculated as €1,272.95, and labor costs accounted for approximately 49.5% of the total operating cost, making them the largest cost component (Asciuto et al., 2019).

In aquaponic systems, feed, energy, and water are among the key inputs that make up operating costs. In a pilot-scale system analysis conducted by Asciuto et al. (2019), it was determined that these three expense items accounted for approximately 19% of total operating costs. This finding demonstrates that energy, feed, and water consumption have a significant impact on system operating costs and that the efficient management of these inputs is critical to system sustainability.

Overall, operating costs in aquaponic systems are determined by labor, water, feed, energy, and system management, and controlling these cost items is critical to the system's economic success (Zappernick et al., 2022; Asciuto et al., 2019). While labor and feed costs, in particular, account for a large portion of total costs, energy consumption also represents a significant operational burden (Zappernick et al., 2022; Asciuto et al., 2019).

3. Resource Efficiency in Aquaponics

The literature indicates that the design and operational performance of aquaponic systems are evaluated primarily in terms of water use efficiency, energy consumption, and nutrient utilization rates (Guan et al., 2025; Ayer & Tyedmers, 2009; Love et al., 2015; Espada Sanjurjo et al., 2026; Delaide et al., 2017; Shnel et al., 2002; Zhu et al., 2025; Nishanth et al., 2025). In this context, various studies presenting data on the energy and water consumption of aquaponic systems were reviewed to assess the current state of these systems and identify areas for improvement.

3.1. Energy Consumption

Energy consumption in aquaponic systems varies depending on the system scale (Guan et al., 2025; Love et al., 2015; Espada Sanjurjo et al., 2026). In a study conducted on an industrial scale with a high level of automation, where water quality was continuously monitored via sensors, and the system consisted of a complex structure comprising modules such as biofilters and aerobic and anaerobic treatment units (Guan et al., 2025), it was reported that the system has a production capacity of 114,700 kg of fish and 97,117 kg of vegetables, and that its annual electricity consumption is approximately 400,000 kWh/year. It has also been noted that a large portion of the system's electricity consumption is attributable to water circulation, greenhouse climate control, and lighting systems (Guan et al., 2025). The energy-consuming components of this system and their respective energy consumption levels are listed in Table 1 (Guan et al., 2025).

Table 1. Electricity consumption of major system components in an industrial-scale aquaponic facility (Guan et al., 2025)

Energy-consuming component	Electricity consumption
Fish rearing operations	16,420 kWh/year
Greenhouse climate control systems	151,728 kWh/year
Water recirculation	126,943 kWh/year
Auxiliary workshop facilities	35,913 kWh/year
Ventilation fans	46,417 kWh/year
Backup lighting	26,888 kWh/year

An examination of Table 1 reveals that, regardless of system scale, climate control systems account for the highest energy consumption in aquaponic production (Guan et al., 2025). In this regard, it has been reported that in a small-scale aquaponic system installed in a region with a cold climate, total annual energy consumption was approximately 19,500 kWh, and that the majority of this consumption was due to in-tank water heaters (Love et al., 2015). This finding suggests that the economic sustainability of fish production in cold climates may be limited. The same study reported that 1 kg of tilapia live weight gain and 1 kg of plant product required 159 kWh and 56 kWh of energy, respectively (Love et al., 2015). Table 2 shows the energy consumption required to produce 1 kg of plants in a small-scale aquaponic system, broken down by season (Love et al., 2015).

Table 2. Seasonal electricity consumption per kilogram of crop production in a small-scale aquaponic system (kWh/kg crops) (Love et al., 2015)

Year	Winter	Spring	Summer	Autumn
2013	298	23	12	89
2014	169	15	14	70

A review of Table 2 reveals that electricity consumption during the fall and winter seasons is significantly higher than in other seasons. Studies examining energy consumption in aquaponic systems integrated with RAS systems have shown that energy consumption values vary depending on different system scales and design approaches, and that energy requirements are one of the primary operational parameters (Delaide et al., 2017; Espada Sanjurjo et al., 2026). In a laboratory-scale aquaponic system, it has been reported that a total of 2,641 kWh of electrical energy was consumed over a 71-day period during which energy consumption was measured, with a daily average of 37 kWh (Delaide et al., 2017). In a small-scale aquaponic system integrating the Nutrient Film Technique (NFT) and a RAS system, it has been reported that energy consumption amounts to 3,062.80 kWh/year for the production of 1 metric ton of plants and fish, and that 52% of this consumption (1,605.20 kWh/year) can be met through photovoltaic systems (Espada Sanjurjo et al., 2026).

When the findings are evaluated collectively, it is evident that while energy consumption varies depending on the scale of the designed aquaponic systems, the climatic characteristics of the region where the system is installed also play a decisive role in energy consumption (Love et al., 2015). In addition, it has been observed that aquaponic systems consume significant amounts of energy through their climate control systems (Guan et al., 2025; Love et al., 2015). In this regard, energy consumption data obtained from various studies in the literature are summarized in Table 3 (Guan et al., 2025; Love et al., 2015; Delaide et al., 2017; Espada Sanjurjo et al., 2026).

Table 3. Comparison of energy consumption data reported for different aquaponic systems

System Scale	Energy Consumption	Key Findings	Reference
Industrial-scale	3.5 kWh/kg fish	In the case of a large-scale aquaponic system, electricity consumption and fish feed usage were identified as the most significant sources of environmental impact.	Guan et al. (2025)
Small-scale	159 kWh/kg fish	Most of the energy consumption came from water heating systems, and fish production required more energy than plant production.	Love et al. (2015)
Pilot-scale	37 kWh/day	It has been recommended that water heating systems and pump operations be optimized to reduce energy consumption.	Delaide et al. (2017)
Pilot-scale	3.06 kWh/kg fish	In the aquaponic system, the use of a photovoltaic system has reduced grid electricity consumption and improved environmental performance.	Espada Sanjurjo et al. (2026)

When the data presented in Table 3 are examined together, it is observed that energy consumption values in aquaponic systems vary over a wide range, from 3.5 kWh/kg of fish to 159 kWh/kg of fish, and that in some studies, energy consumption values are reported using different units (Guan et al., 2025; Love et al., 2015; Espada Sanjurjo et al., 2026; Delaide et al., 2017). At this point, differences in the units used for reporting the data limit the comparability of the systems. Furthermore, studies show that energy consumption per kilogram of fish varies depending on the scale of the system, the climatic conditions where the system is located, and the technologies used (Guan et al., 2025; Love et al., 2015; Espada Sanjurjo et al., 2026). It is particularly noteworthy that energy consumption per unit of production increases significantly in small-scale systems (Love et al., 2015). In contrast, energy efficiency is found to be higher in large-scale, optimized systems (Guan et al., 2025). This difference stems from increased resource utilization efficiency in large-scale systems and improved system design.

3.2. Water Consumption

Water management in aquaponic systems is one of the most critical design and operational parameters in terms of the system's sustainability and efficiency. In the study by Shnel et al. (2002), the zero-discharge recirculating aquaculture system (RAS) approach developed for aquaculture systems presents a significant design innovation in terms of water management by integrating nitrification (trickling filter) and denitrification (anoxic reactor) processes in addition to the conventional RAS components. It has been reported that this system consumes 190 L of water to produce 1 kg of fish and that the system can operate stably even at high stocking densities (Shnel et al., 2002). Furthermore, the system's long-term (331-day) operational performance demonstrates that water quality can be maintained at sustainable levels despite high stocking densities (61.8 kg/m^3) (Shnel et al., 2002). This demonstrates that closed-loop systems can operate stably over the long term with proper design and process integration.

Research is being conducted on multi-cycle and integrated system designs to improve resource efficiency in aquaponic systems. In this context, in the study by Zhu et al. (2025), the aquaponic system, unlike conventional systems, was designed as a multi-loop model in which a recirculating aquaculture system (RAS), a hydroponic production tank, an anaerobic digester, and a desalination unit operate in combination. This approach makes it possible to optimize system performance through water, energy, and nutrient balances. According to the results of the optimization scenarios, it has been reported that the system can achieve water use efficiency of up to 97% and phosphorus use efficiency of up to

96%, and that the system's daily freshwater input requirement can be reduced to as low as 1.5 L/m² (Zhu et al., 2025). The flow diagram of the aquaponic system designed in this study is shown in Figure 2.

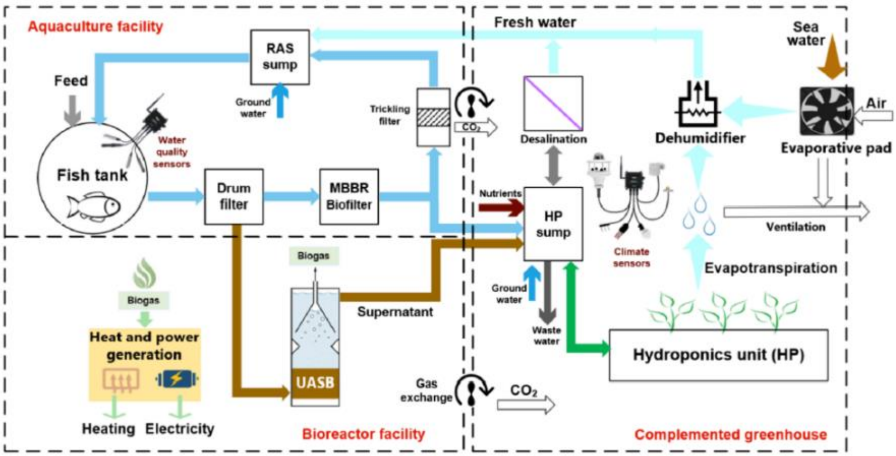

Figure 2. Flowchart of an aquaponic system (Zhu et al., 2025)

A review of Figure 2 reveals that the system is designed as a multi-loop structure consisting of a recirculating aquaculture system (RAS), a plant cultivation unit, an anaerobic digester, and a desalination unit; water, nutrient, and energy flows are managed in an integrated manner among these components. Upon detailed examination of the flow diagram, it can be seen that the aquaculture section features a circulation system consisting, in order, of a fish tank, a drum filter, an MBBR biofilter, and a trickle filter (Zhu et al., 2025). The innovative approach in the study by Zhu et al. (2025) involves directing the sludge separated from the drum filter to UASB anaerobic digesters, thereby converting the nitrogen and phosphorus in the sludge back into soluble forms and producing biogas. In addition, the liquid fraction produced in UASB anaerobic digesters is directed to hydroponic sump units and from there to plant cultivation units, thereby enabling nutrient recovery from the sludge (Zhu et al., 2025). Furthermore, in the study by Zhu et al. (2025), unlike conventional aquaponic systems, a desalination unit was added to the flow diagram; the nutrient solution collected in the hydroponic sump unit undergoes desalination, and the nutrient-rich liquid is returned to the hydroponic system, while the freshwater is returned to the RAS.

In an example of an industrial-scale aquaponic system, similar to the study by Zhu et al. (2025), it was reported that water reuse efficiency exceeded 90% and that approximately 114,700 kg of fish were produced using 24,900 m³ of water annually; based on these data, the specific water consumption was calculated to be approximately 217 L/kg of fish (Guan et al., 2025). These findings indicate that, despite the high energy requirements of aquaponic systems, they offer significantly higher water use efficiency compared to traditional agriculture and aquaculture systems (Shnel et al., 2002; Zhu et al., 2025; Guan et al., 2025). Furthermore, the high water efficiency achieved in the study by Guan et al. (2025) serves as an example of how low water consumption can be achieved in large-scale systems through well-designed water recovery technologies.

Studies conducted on small-scale systems also provide important quantitative data on water use (Love et al., 2015; Delaide et al., 2017). For example, it has been determined that in a small-scale aquaponic system with a volume of approximately 10.3 m^3, daily water loss is about 1%, and this loss is offset by adding approximately 36 m^3 of water per year (Love et al., 2015). When the same study was evaluated in terms of production efficiency, it was determined that water consumption amounted to 104 L and 292 L, respectively, for the production of 1 kg of crop yield and 1 kg of live weight gain (Love et al., 2015). Delaide et al. (2017) calculated that a small-scale aquaponic system consumed 244 L of water to produce 1 kg of vegetables and 278 L to achieve a 1 kg weight gain in tilapia, and noted that a 3.6% daily water exchange rate occurred. In the studies by Love et al. (2015) and Delaide et al. (2017), the daily addition of water to overcome water loss emerges as a factor that increases water consumption. When the studies examined are evaluated collectively, it is evident that aquaponic systems offer high water-use efficiency by significantly reducing water consumption per unit of production through water recirculation and recovery (Shnel et al., 2002; Guan et al., 2025; Zhu et al., 2025; Love et al., 2015; Delaide et al., 2017). Table 4 summarizes water consumption data obtained from various studies in the literature (Shnel et al., 2002; Guan et al., 2025; Zhu et al., 2025; Love et al., 2015; Delaide et al., 2017).

Table 4. Water consumption data obtained from various studies in the literature

System Scale	Water Consumption	Key Findings	Reference
Pilot-scale / Semi-commercial	190 L/kg fish	Thanks to the zero-discharge recirculation system, water consumption has been maintained at 190 L/kg of fish, and water use efficiency has been improved.	Shnel et al. (2002)
Industrial-scale	217 L/kg fish	In the industrial aquaponic system, water consumption was achieved at 217 L/kg of fish through the reuse of water in a closed loop, and the system demonstrated high water efficiency.	Guan et al. (2025)
Industrial-scale	580–630 L/kg fish	In an industrial aquaponic system optimized for arid regions, water use efficiency reached 97%, while water consumption was determined to be in the range of 580–630 L/kg of fish.	Zhu et al. (2025)
Small-scale	104 L/kg crops 292 L/kg fish	In a small-scale aquaponic system, plant production was carried out with lower water consumption compared to fish production, demonstrating the efficient use of water.	Love et al. (2015)
Small-scale / Pilot-scale	278 L/kg fish	In the PAFF Box aquaponic system, water consumption for fish production was determined to be 278 L/kg, and it was emphasized that water use is efficient.	Delaide et al. (2017)

A review of Table 4 reveals that water consumption per unit of production in aquaponic systems varies widely for fish production, ranging from 190 L/kg of fish to 630 L/kg of fish (Shnel et al., 2002; Guan et al., 2025; Zhu et al., 2025; Love et al., 2015; Delaide et al., 2017). The main reasons for the differences in water consumption among these systems are their differing design approaches, the inclusion of water recovery technologies in some systems, and variations in water exchange rates depending on climatic conditions (Shnel et al., 2002; Guan et al., 2025; Zhu et al., 2025; Love et al., 2015; Delaide et al., 2017). Nevertheless, it is evident that water use efficiency is high in all systems thanks to their closed-loop design, which is based on the principle of water reuse.

4. Fish Sludge Management and Resource Recovery

Aquaponic systems are closed-loop production systems that enable the recovery of nutrients from wastewater and sludge (Lennard & Goddek, 2019). In these systems, the nitrogen contained in fish waste is converted by microorganisms through the nitrification process into a form that can be absorbed by plants, thereby serving as an important nutrient source (Kim et al., 2005). In addition, fish sludge separated by mechanical filtration can be returned to the system through the mineralization of the nutrients it contains, which converts them into a soluble form (Goddek et al., 2015). As a result, the need for additional chemical fertilizers within the system can be significantly reduced (Love et al., 2015).

However, the literature indicates that nutrient recovery in aquaponic systems does not occur in a fully closed-loop manner (Love et al., 2015; Delaide et al., 2017). In this context, it is noted that the sludge containing valuable nutrients produced in the aquaponic system is not directly recycled within the system but is removed from the system through mechanical filtration (Love et al., 2015). It has also been reported that approximately 50–88% of nutrients can be lost from the system due to sludge removal processes (Delaide et al., 2017). When the nutrient ratios available to plants within the system were examined, it was determined that approximately 36% of the nitrogen and 49% of the phosphorus were taken up by the plants (Espada Sanjurjo et al., 2026). These findings indicate that while aquaponic systems provide nutrient recovery, they have not yet achieved a fully closed loop.

In aquaponic systems, both the liquid phase and the sludge phase are crucial for nutrient recovery. Accordingly, it has been determined that sludge from aquaponic systems contains approximately 2.85–3.07% nitrogen on a dry matter basis (Hindelang et al., 2014). It has also been reported that in the sludge fraction from aquaculture, up to 32% of total nitrogen and up to 84% of total phosphorus can be retained (Zhang et al., 2021; Cripps & Bergheim, 2000). Nevertheless, in most existing systems, sludge is discharged directly outside the system, resulting in significant nutrient losses (Zhang et al., 2021). For this reason, sludge recovery is considered a critical factor in maintaining the nutrient cycle in aquaponic systems.

One of the most common approaches to increasing nutrient recovery from sludge is to mineralize the sludge using anaerobic and aerobic digestion systems, thereby converting it into a soluble form (Zhu et al., 2025; Lian et al., 2024; Madady et al., 2025). Through anaerobic digestion, approximately 90% of the phosphorus and 86% of the nitrogen in the sludge can be converted into soluble forms (Zhu et al., 2025). In aerobic systems, on the other hand, higher solids removal is achieved while the recovery of soluble nutrients is also increased (Lian et al., 2024). The liquid phase obtained as a result of these processes can be reused as liquid fertilizer in hydroponic systems (Madady et al., 2025).

One of the innovative applications developed for nutrient recovery from aquaponic sludge involves converting the sludge into liquid fertilizer through aerobic digestion (Madady et al., 2025). The fertilizer produced using this method contains 16.5 mg/L of phosphate, 20.25 mg/L of nitrate, and 68.64 mg/L of potassium, and returning this solution to the system significantly enhances plant growth (Madady et al., 2025).

Integrated approaches that combine various methods for nutrient recovery are also becoming increasingly important (Nishanth et al., 2025). In this context, physical methods such as sedimentation, filtration, and membrane technologies are used as pretreatment for solid-liquid separation; among chemical methods, struvite precipitation and ion exchange stand out; and biological methods, in which microorganisms break down organic matter and convert nutrients into forms usable by plants, play an important role in nutrient recovery (Nishanth et al., 2025). It has been reported that hybrid systems, which combine these methods, offer significant advantages in improving nutrient recovery efficiency and system performance (Nishanth et al., 2025).

In systems developed on an industrial scale, nutrient recovery is carried out through multi-stage, integrated processes (Guan et al., 2025; Zhu et al., 2025). The liquid and solid phases separated from the sludge are processed separately, converted into a nutrient solution through aerobic and anaerobic biological processes, and the resulting solution is reused in hydroponic production (Guan et al., 2025). In addition, system efficiency is enhanced by optimizing nutrient concentrations through multi-cycle system designs that integrate desalination, anaerobic digestion, and water recovery processes (Zhu et al., 2025). In this context, it has been reported that, as a result of improvements to the system design, phosphorus use efficiency and water use efficiency reached 96% and 97%, respectively (Zhu et al., 2025). Such system approaches allow aquaponics systems to operate more closely to a closed-loop nutrient management system.

In addition, alternative uses for sludge also offer significant opportunities for nutrient recovery (El-Kady & Suloma, 2025). The use of aquaculture sludge as organic fertilizer enhances plant growth and reduces the use of chemical fertilizers (El-Kady & Suloma, 2025). In addition, the conversion of sludge into biomass through insect larvae and other organisms is emerging as an important approach to nutrient recovery (Pettersen et al., 2025). However, the presence of heavy metals, pathogens, and other contaminants in these processes is a significant limiting factor that must be addressed in terms of food and feed safety (Pettersen et al., 2025).

In conclusion, nutrient recovery from wastewater and sludge in aquaponic systems plays a critical role in efficient resource use. While current systems achieve significant recovery, there is a need for integrated and innovative technologies to reduce nutrient losses and make more effective use of the sludge fraction. Systems developed along these lines, which combine biological, chemical, and physical processes, make a significant contribution to enhancing the sustainability of aquaponic production (Nishanth et al., 2025).

5. Conclusions

Aquaponic systems are among the innovative production technologies that integrate fish and plant production, transforming water, energy, and nutrients within the system into a valuable resource (Lennard & Goddek, 2019; Joyce et al., 2019). The studies examined in this chapter of the book demonstrate that system design, investment and operating costs, energy consumption, water use efficiency, and fish sludge management are key factors determining the performance of aquaponic systems (Love et al., 2015; Lennard & Goddek, 2019; Zhu et al., 2025).

Effective management of fish sludge and nutrient recovery are critical to the development of aquaponic systems in line with the principles of the circular economy. Studies in the literature show that a significant portion of nutrients in existing systems is retained in the sludge phase and, therefore, anaerobic and aerobic mineralization, liquid organic fertilizer production, hybrid nutrient recovery technologies, and multi-cycle system designs offer significant opportunities for returning nutrients to the system (Guan et al., 2025; Zhu et al., 2025; Madady et al., 2025; Nishanth et al., 2025). However, when developing alternative uses for sludge, it is also necessary to take into account food and feed safety risks associated with contaminants such as heavy metals and pathogens (Pettersen et al., 2025).

Despite the valuable findings reported in the literature, certain limitations should be taken into account when interpreting the results. While the studies reviewed provide important insights regarding the design, energy, water, and nutrient recovery of aquaponic systems, they differ in terms of system scale, the climatic conditions under which the systems were established, the level of innovation in system designs, operational durations, and the units used to report quantitative data (Guan et al., 2025; Love et al., 2015; Zhu et al., 2025; Espada Sanjurjo et al., 2026; Delaide et al., 2017; Shnel et al., 2002). While this situation provides diversity by allowing for the evaluation of a similar topic from different perspectives, it also limits the ability to draw common conclusions across studies. For example, while the study by Espada Sanjurjo et al. (2026) presents data on energy consumption in kWh/year, the study by Love et al. (2015) uses kWh/kg of fish as the unit. Furthermore, while the study by Delaide et al. (2017) evaluated a 71-day operating period, the study by Shnel et al. (2002) evaluated a 331-day operating period, making it difficult to make direct quantitative comparisons between the studies.

In conclusion, enhancing the sustainability of aquaponic systems is not limited to the development of water-saving production systems; it also depends on increasing the use of renewable energy, reducing investment and operating costs, and developing improved system designs that recover nutrients to the highest possible extent (Nishanth et al., 2025; Zhu et al., 2025; Guan et al., 2025; Espada Sanjurjo et al., 2026; Zappernick et al., 2022). It is recommended that future studies focus on developing standard energy and water consumption reporting protocols for different climate conditions and production scales, and on evaluating sludge recovery technologies through life-cycle cost analysis.

Acknowledgement

This study was supported by the Scientific and Technological Research Council of Türkiye (TÜBİTAK) as part of the international project titled "Interdisciplinary research to ensure the availability of quality water and food, generating, transferring knowledge and solutions that promote entrepreneurship and sustainable water management of micro, medium and small-scale biointegrated agro-aqua-culture systems," project number 124N067. The authors would like to thank the funding agency for its financial support of the project.

6. References

Asciuto, A., Schimmenti, E., Cottone, C., & Borsellino, V. (2019). A financial feasibility study of an aquaponic system in a Mediterranean urban context. *Urban Forestry & Urban Greening*, *38*, 397-402. https://doi.org/10.1016/j.ufug.2019.02.001

Ayer, N. W., & Tyedmers, P. H. (2009). Assessing alternative aquaculture technologies: Life cycle assessment of salmonid culture systems in Canada. *Journal of Cleaner Production*, *17*(3), 362-373. https://doi.org/10.1016/j.jclepro.2008.08.002

Babatunde, A., Deborah, R., Gan, M., & Simon, T. (2021). Economic viability of a small scale low-cost aquaponic system in South Africa. *Journal of Applied Aquaculture*, *35*(2), 285-304. https://doi.org/10.1080/10454438.2021.1958729

Cripps, S. J., & Bergheim, A. (2000). Solids management and removal for intensive land-based aquaculture production systems. *Aquacultural Engineering*, *22*(1-2), 33-56. https://doi.org/10.1016/S0144-8609(00)00031-5

Delaide, B., Delhaye, G., Dermience, M., Gott, J., Soyeurt, H., & Jijakli, M. H. (2017). Plant and fish production performance, nutrient mass balances, energy and water use of the PAFF Box, a small-scale aquaponic system. *Aquacultural Engineering*, *78*, 130-139. https://doi.org/10.1016/j.aquaeng.2017.06.002

El-Kady, A. F. Y., & Suloma, A. (2025). Sediment management in integrated aquaculture-agriculture systems: Sustainable use of fish culture sludge for organic fertilization of *Terminalia arjuna*. *Environmental Science and Pollution Research*, *32*, 4273-4287. https://doi.org/10.1007/s11356-025-35910-w

Espada Sanjurjo, J. J., Díaz de Mera-Sánchez, M. P., & Rodríguez Escudero, R. (2026). Design and environmental analysis of an aquaponics system coupled with photovoltaic unit for food production and reuse of nutrients from wastewater: A life cycle assessment study. *Applied Sciences*, *16*(2), 635. https://doi.org/10.3390/app16020635

Espinal, C. A., & Matulić, D. (2019). Recirculating aquaculture technologies. In: Goddek, S., Joyce, A., Kotzen, B., Burnell, G.M. (Eds), *Aquaponics food production systems: Combined aquaculture and hydroponic production technologies for the future* (pp. 35-76). Springer. https://doi.org/10.1007/978-3-030-15943-6_3

Goddek, S., Delaide, B., Mankasingh, U., Ragnarsdottir, K. V., Jijakli, H., & Thorarinsdottir, R. (2015). Challenges of sustainable and commercial aquaponics. *Sustainability*, *7*(4), 4199-4224. https://doi.org/10.3390/su7044199

Godfray, H. C. J., Beddington, J. R., Crute, I. R., Haddad, L., Lawrence, D., Muir, J. F., Pretty, J., Robinson, S., Thomas, S. M., & Toulmin, C. (2010). *Food Security: The Challenge of Feeding 9 Billion People*. Science, *327*(5967), 812–818. https://doi.org/10.1126/science.1185383

Guan, Y., Liu, L., Chen, Y., & Liu, L. (2025). Life cycle assessment of an industrial aquaponics system in Chongqing, China: Environmental performance and optimization strategies. *Sustainability*, *17*(18), 8254. https://doi.org/10.3390/su17188254

Hindelang, M., Gheewala, S. H., Mungkung, R., & Bonnet, S. (2014). Environmental sustainability assessment of a media based aquaponics system in Thailand. *Journal of Sustainable Energy & Environment*, *5*, 109-116.

Hu, Z., Lee, J. W., Chandran, K., Kim, S., Brotto, A. C., & Khanal, S. K. (2015). Effect of plant species on nitrogen recovery in aquaponics. *Bioresource Technology*, *188*, 92-98. https://doi.org/10.1016/j.biortech.2015.01.013

Ibrahim, L. A., Shaghaleh, H., El-Kassar, G. M., Abu-Hashim, M., Elsadek, E. A., & Alhaj Hamoud, Y. (2023). Aquaponics: A sustainable path to food sovereignty and enhanced water use efficiency. *Water*, *15*(24), 4310. https://doi.org/10.3390/w15244310

Joyce, A., Goddek, S., Kotzen, B., Wuertz, S., 2019. Aquaponics: closing the cycle on limited water, land and nutrient resources. In: Goddek, S., Joyce, A., Kotzen, B., Burnell, G.M. (Eds), *Aquaponics Food Production Systems: Combined Aquaculture and Hydroponic Production Technologies for the Future* (pp. 19-34). Springer. https://doi.org/10.1007/978-3-030-15943-6_2

Kim, D.-J., Ahn, D. H., & Lee, D.-I. (2005). Effects of free ammonia and dissolved oxygen on nitrification and nitrite accumulation in a biofilm airlift reactor. *Korean Journal of Chemical Engineering*, *22*, 85–90. https://doi.org/10.1007/BF02701467

Lennard, W., & Goddek, S. (2019). Aquaponics: The basics. In: Goddek, S., Joyce, A., Kotzen, B., Burnell, G.M. (Eds), *Aquaponics food production systems: Combined aquaculture and hydroponic production technologies for the future* (pp. 113-143). Springer. https://doi.org/10.1007/978-3-030-15943-6_5

Lian, J., He, Y., Wang, L., Liu, Y., Wang, K., Sunde, J., Rebours, C., Liu, H., Zhu, X., Han, D., Hu, Q., & Li, M. (2024). Recovery of nutrients from fish sludge to enhance the growth of microalga *Chlorella sorokiniana*

CMBB276. *Marine Pollution Bulletin*, *203*, 116421. https://doi.org/10.1016/j.marpolbul.2024.116421

Love, D. C., Uhl, M. S., & Genello, L. (2015). Energy and water use of a small-scale raft aquaponics system in Baltimore, Maryland, United States. *Aquacultural Engineering*, *68*, 19-27. https://doi.org/10.1016/j.aquaeng.2015.07.003

Madady, M. H., Sarkheil, M., Zahedi, S., & Arouei, H. (2025). Application of liquid organic fertilizer produced from fish sludge in an aquaponics system: Influences on growth of Nile tilapia (*Oreochromis niloticus*) and peppermint (*Mentha piperita* L.). *Aquacultural Engineering*, *110*, 102541. https://doi.org/10.1016/j.aquaeng.2025.102541

Nishanth, D., Somanathan Nair, C., Manoharan, R., Subramanian, R., Salim, I., Maqsood, S., & Jaleel, A. (2025). Current technologies for nutrient recovery in aquaponic systems: A review. *Frontiers in Sustainable Food Systems*, *9*, e1681638. https://doi.org/10.3389/fsufs.2025.1681638

Petrea, S. M., Coadă, M. T., Cristea, V., Dediu, L., Cristea, D., Rahoveanu, A. T., Zugravu, A. G., Rahoveanu, M. M. T., & Mocuta, D. N. (2016). A comparative cost-effectiveness analysis in different tested aquaponic systems. *Agriculture and Agricultural Science Procedia*, *10*, 555-565. https://doi.org/10.1016/j.aaspro.2016.09.034

Pettersen, K. S., Sele, V., Araujo, P., Belghit, I., Benestad, S. L., Bernhoft, A., Booth, A. M., Eriksen, G. S., Farkas, J., Handå, A. H., Hansen, B. H., Helgesen, K. O., Holst-Jensen, A., Johannessen, G. S., Liland, N. S., Lundebye, A.-K., Malzahn, A. M., Nilsen, H., Nordtvedt, T. S., . . . Hagemann, A. (2025). Fish sludge as feed in circular bioproduction: Overview of biological and chemical hazards in fish sludge and their potential fate via ingestion by invertebrates. *Reviews in Aquaculture*, *17*(1), e12996. https://doi.org/10.1111/raq.12996

Shnel, N., Barak, Y., Ezer, T., Dafni, Z., & van Rijn, J. (2002). Design and performance of a zero-discharge tilapia recirculating system. *Aquacultural Engineering*, *26*(3), 191-203. https://doi.org/10.1016/S0144-8609(02)00013-4

Somerville, C., Cohen, M., Pantanella, E., Stankus, A., & Lovatelli, A. (2014). *Small-scale aquaponic food production: Integrated fish and plant farming* (FAO Fisheries and Aquaculture Technical Paper No. 589). Food and Agriculture Organization of the United Nations.

United Nations Department of Economic and Social Affairs, Population Division. (2022). World population prospects 2022: Summary of results (UN DESA/POP/2022/TR/NO. 3). United Nations.

https://www.un.org/development/desa/pd/sites/www.un.org.development.desa.pd/files/wpp2022_summary_of_results.pdf

Zappernick, N., Nedunuri, K. V., Islam, K. R., Khanal, S., Worley, T., Laki, S. L., & Shah, A. (2022). Techno-economic analysis of a recirculating tilapia-lettuce aquaponics system. *Journal of Cleaner Production*, *365*, 132753. https://doi.org/10.1016/j.jclepro.2022.132753

Zhang, H., Gao, Y., Liu, J., Lin, Z., Lee, C. T., Hashim, H., Wu, W.-M., & Li, C. (2021). Recovery of nutrients from fish sludge as liquid fertilizer to enhance sustainability of aquaponics: A review. *Chemical Engineering Transactions*, *83*, 55-60. https://doi.org/10.3303/CET2183010

Zhu, Z., Yogev, U., Gross, A., & Keesman, K. J. (2025). Environmental assessment of industrial aquaponics in arid zones using an integrated dynamic model. *Information Processing in Agriculture*, *12*, 260-277. https://doi.org/10.1016/j.inpa.2024.09.005